Current Topics

Atomic Force Microscopy Studies of Native Photosynthetic Membranes[†]

James N. Sturgis,[‡] Jaimey D. Tucker,[§] John D. Olsen,[§] C. Neil Hunter,[§] and Robert A. Niederman*,[ll]

*Laboratoire d'Ingénierie des Systèmes Macromoléculaires, UPR 9027, Aix Marseille Université, 31 Chemin Joseph Aiguier,
13402 Marseilles, France, Department of Molecular Biology and Biotechnology, University of Sheffield, Sheffield S10 2TN, U.K., and
Department of Molecular Biology and Biochemistry, Rutgers University, Piscataway, New Jersey 08854-8082*

ABSTRACT: In addition to providing the earliest surface images of a native photosynthetic membrane at submolecular resolution, examination of the intracytoplasmic membrane (ICM) of purple bacteria by atomic force microscopy (AFM) has revealed a wide diversity of species-dependent arrangements of closely packed light-harvesting (LH) antennae, capable of fulfilling the basic requirements for efficient collection, transmission, and trapping of radiant energy. A highly organized architecture was observed with fused preparations of the pseudocrystalline ICM of *Blastochloris viridis*, consiting of hexagonally packed monomeric reaction center light-harvesting 1 (RC-LH1) core complexes. Among strains which also form a peripheral LH2 antenna, images of ICM patches from *Rhodobacter sphaeroides* exhibited well-ordered, interconnected networks of dimeric RC-LH1 core complexes intercalated by rows of LH2, coexisting with LH2-only domains. Other peripheral antenna-containing species, notably *Rhodospirillum photometricum* and *Rhodopseudomonas palustris*, showed a less regular organization, with mixed regions of LH2 and RC-LH1 cores, intermingled with large, paracrystalline domains. The ATP synthase and cytochrome bc_1 complex were not observed in any of these topographs and are thought to be localized in the adjacent cytoplasmic membrane or in inaccessible ICM regions separated from the flat regions imaged by AFM. The AFM images have served as a basis for atomic-resolution modeling of the ICM vesicle surface, as well as forces driving segregation of photosynthetic complexes into distinct domains. Docking of atomic-resolution molecular structures into AFM topographs of *Rsp. photometricum* membranes generated precise in situ structural models of the core complex surrounded by LH2 rings and a region of tightly packed LH2 complexes. A similar approach has generated a model of the highly curved LH2-only membranes of *Rba. sphaeroides* which predicts that sufficient space exists between LH2 complexes for quinones to diffuse freely. Measurement of the intercomplex distances between adjacent LH2 rings of *Phaeospirillum molischianum* has permitted the first calculation of the separation of bacteriochlorophyll *a* molecules in the native ICM. A recent AFM analysis of the organization of green plant photosystem II (PSII) in grana thylakoids revealed the protruding oxygen-evolving complex, crowded together in parallel alignment at three distinct levels of stacked membranes over the lumenal surface. The results also confirmed that PSII−LHCII supercomplexes are displaced relative to one another in opposing grana membranes.

In recent years, atomic force microscopy (AFM)[1] has become an important tool for assessing the submolecular surface architecture of integral protein complexes in their native membrane environments. Because of the high signal-

[1] Abbreviations: AFM, atomic force microscopy; BChl, bacteriochlorophyll *a*; CM, cytoplasmic membrane; ICM, intracytoplasmic membrane; LD, linear dichroism; LH1, core light-harvesting complex, containing a dimeric BChl ellipse in *Rhodobacter sphaeroides*, absorbing near 875 nm, designated as B875 BChl; LH2, peripheral light-harvesting complex, which in *Rba. sphaeroides* contains a monomeric BChl ring absorbing at 800 nm and a dimeric BChl ring absorbing at 850 nm, designated as B800 and B850 BChl, respectively; RC, photochemical reaction center.

to-noise ratio provided by AFM, which is vastly superior to that of optical microscopy, in situ topographs can be acquired with a vertical resolution approaching ~1 Å and a lateral resolution of ~10 Å, under essentially native physiological conditions (i.e., in buffer solution at ambient pressure and temperature). Foremost among these efforts are recent innovative AFM studies on the intracytoplasmic membrane (ICM) of purple, anoxygenic photosynthetic bacteria (*1–4*), which as the first surface views of the organization of multicomponent biological membranes at submolecular resolution represent an important breakthrough in structural biology. These remarkable images have also served as a critical test for long-standing models of the arrangement of densely packed photosynthetic complexes within the ICM, based upon transmission electron microscopy (TEM) (*5–7*), as well as excitation annihilation studies (*8–10*). Moreover, the resulting AFM topographs have demonstrated how a considerable diversity in structural organization among different species can fulfill the basic requirements for efficient collection, transmission, and trapping of radiant energy over the extensive surface areas provided by a variety of distinct ICM structures, functioning in diverse ecological niches.

These AFM images of the in situ organization of the reaction center (RC) and light-harvesting (LH) complexes, together with the availability of their X-ray structures (*11–13*), have also served as the basis for atomic-level modeling of these supramolecular assemblies in their native membrane environment (*14*), as well as the determination of precise in situ distances between bacteriochlorophyll *a* (BChl) molecules in neighboring LH2 complexes (*15*). In addition, the local structural arrangement of the LH and RC complexes observed by AFM (*16*) has been extended into a long-range description of their organization over the surface of an ICM (chromatophore) vesicle by linear dichroism (LD) measurements of the difference between horizontally and vertically polarized light relative to the orientation axis in membranes embedded in stretched films (*17–19*). This combination of AFM and LD results has been used in evaluating the forces that drive domain formation and curvature in the ICM (*19*), as well as a global effort in which the structural and functional organization of the protein surface of an entire biological membrane vesicle has been precisely modeled for the first time at atomic resolution (*20, 21*). Additionally, recent AFM images of flattened pieces of LH2-only membranes of *Rhodobacter sphaeroides* have led to a functional model of highly curved native membranes, which indicate that these structures would permit the free diffusion of electron carriers through the LH2 domains, while still maintaining efficient excitation energy transfer (*22*).

A critical assessment of the important developments arising from ongoing AFM studies on the molecular organization of the LH and RC components in the native ICM of a number of purple photosynthetic bacteria is presented here, together with their significant structural and functional implications. The recent extension of this new epoch in membrane structural biology to the supramolecular architecture of the multiprotein complexes in chloroplast thylakoid membranes is also discussed. In addition, novel methods for the identification of components visualized at the membrane surface in AFM topographs will be considered, as well as the prospects that AFM, in conjunction with other innovative techniques, holds for future studies.

USING AFM TO STUDY BIOLOGICAL MEMBRANES

The atomic force microscope is able to map out the surface topography of biological membranes with impressive precision (*1*). The key element of the AFM is a pyramidal tip that touches the sample surface. This tip is attached to a cantilever; deflections of the cantilever due to forces as little as 10 pN can be detected by an optical system composed of a laser and sectored detector. A topographic image is acquired by raster scanning the sample below the tip, using a piezoelectric scanner coupled to a feedback system that displaces the sample vertically to keep the cantilever deflection, and thus the sample–tip interaction force, constant. An important advantage of this type of microscope is the possibility of using it in solution, i.e., with the sample and tip immersed in buffer. Thus, measurements can be made under near-native conditions in an aqueous environment. However, the electrostatic component of tip–sample interactions is very important, and thus, the ionic strength and composition of the scanning buffer are critical in determining the quality of the resulting images.

Two different modes of operation are regularly employed for studying protein organization in biological membranes: contact mode and oscillating mode (*1*). In contact mode, the tip presses on the sample with a constant force, typically of ~100 pN; this mode usually gives slightly higher resolution but results in strong frictional forces and thus requires a relatively robust interaction between the sample and the mica support. In oscillating mode, the cantilever is made to oscillate at a resonant frequency and thus interacts with the sample only at the bottom of each cycle; this mode typically gives slightly lower resolution but produces less friction and thus can be used to study samples less solidly attached to the mica support. An important application arises in contact mode, where the frictional forces can be used for nanodissection of the sample.

AFM STUDIES OF PHOTOSYNTHETIC COMPLEXES AND NATIVE MEMBRANES OF PURPLE BACTERIA

A complete description of the photosynthetic apparatus of purple bacteria requires the determination of both the structure of the individual components at atomic resolution (*12, 13, 23–25*) and their supramolecular structural and functional organization within the native membrane (*1–3*). The high signal-to-noise ratio and lateral resolution provided by AFM facilitate the identification of the components within individual multiprotein complexes, as well as the evaluation of the manner in which complexes are arrayed over the ICM surface. In this section, we present an overview of studies on the peripheral LH2 and LH1 core proteins of purple bacteria, reconstituted into lipid bilayers as densely packed crystals (*26–31*), followed by a critical assessment of pioneering AFM investigations on the organization of photosynthetic complexes within the native membrane.

AFM Studies on Purified LH2 and RC-LH1 Complexes. The earliest AFM analysis of photosynthetic complexes from purple bacteria was performed on densely packed two-dimensional (2D) crystals prepared by reconstituting the purified *Rubrivivax gelatinosus* LH2 protein into lipid bilayers (*26*). A nonameric LH2 ring structure was identified,

along with the membrane protruding domains at the periplasmic and cytoplasmic surfaces, while LH1 rings, present as a minor contaminant, were also observed for the first time at subnanometer resolution using AFM. Much additional structural information has been obtained from subsequent AFM analyses of 2D crystals of LH2 complexes from *Rba. sphaeroides* (*27, 28*) and *Rhodopseudomonas acidophila* (*29, 30*), including an assessment of the implications of protein packing effects arising from protein−protein contacts (*31*), the intrinsic flexibility of individual subunits, and the tendency of reconstituted LH2 to form elliptical and tilted structures. However, the possible physiological implications of these observations awaited direct AFM analysis of the native ICM, free of the packing constraints in the crystals.

AFM has also been performed on 2D crystals reconstituted from the *Rba. sphaeroides* LH1 complexes, purified from membranes lacking both the LH2 and RC complexes, which revealed considerable heterogeneity in LH1 size, as well as larger variations in the shape of the annular structure than in LH2 (*28*). This was ascribed to H-bonding patterns between BChl and the LH1 apoprotein within $\alpha_1\beta_1BChl_2$ protomers, resulting in weaker associations between individual subunits than in LH2 protomers, where interprotomer H-bonding also exists. This apparently dynamic separation of LH1 $\alpha_1\beta_1BChl_2$ subunits could accommodate movement of quinone redox species by transient opening and closing of the LH1 annular ring adjoining the RC Q_B site (see below). Moreover, EM projection maps showed that the *Rba. sphaeroides* RC-LH1 complex is able to adopt both circular and elliptical conformations (*32*), and such inherent LH1 flexibility was also observed by AFM in the closed LH1 annulus surrounding the RC in various 2D crystal forms of reconstituted *Rhodospirillum rubrum* RC-LH1 core complexes (*33*). Nevertheless, the in situ architecture of the RC-LH1 core complex as well as a role for LH1 deformability in the movement of quinone redox species between the RC and cytochrome bc_1 complexes required the demonstration of different LH1 conformations in the native ICM environment by noninvasive AFM procedures. In addition, AFM imaging of native membranes provides definitive structural information about the intactness and conformation of photosynthetic complexes in the absence of the extensive purification, isolation, and reconstitution protocols necessary for the 2D crystallization process.

Preparation of Native Photosynthetic Membranes for AFM Analysis. Because the collection of AFM images of native membranes in buffer solution requires that sufficiently large bilayer expanses form a flat layer closely adhering to the mica support, the ICM of purple bacteria initially posed a number of technical challenges that needed to be overcome before reliable topographs of their surface architecture could be attained. Purple photosynthetic bacteria that have been examined by AFM possess a variety of in vivo ICM arrangements: these include the interconnected vesicular structures in *Rba. sphaeroides* (*16*) and *Rhodobacter blasticus* (*34*), flattened lamellar discs in *Blastochloris viridis* (*35*), and infoldings of the cytoplasmic membrane (CM) that take the form of regular bundles of flattened thylakoid-like discs in *Rhodospirillum photometricum* (*36*) and *Phaeospirillum molischianum* (*15*); in *Rhodopseudomonas palustris* (*37*), this type of architecture has been shown to be differentiated into both stacked and unstacked lamellae (*38*) (see Figure 10A below).

These various ICM morphologies required development of a number of different strategies for obtaining preparations suitable for AFM. Although the vesicular ICM gives rise to closed vesicles (chromatophores) of fairly uniform size upon cellular disruption in a French pressure cell, these structures do not present sufficiently flat areas, unless they are gently disrupted or fused into larger structures. This was accomplished with the chromatophores of *Rba. sphaeroides* by treatment with subsolubilizing amounts of detergent that give rise to flat membrane patches (*16*) or by freeze−thaw induced fusion of *Rba. blasticus* chromatophores (*34*), or the disrupted membrane sheets of *Blc. viridis* (*35*). In the initial studies with *Rsp. photometricum* (*36*), the isolated structures failed to collapse completely out onto the mica surface, and the AFM tip was used to nanodissect away the weakly attached upper vesicle membrane layer, to reveal the periplasmic surface. This proved to be unnecessary in subsequent investigations in this organism (*39*), or in *Phs. molischianum* (*15*) and *Rps. palustris* (*37*), where isolated membrane sacs were deposited directly on the support, allowing visualization of the upper layer (cytoplasmic surface), superimposed on the lower layer, adhering to the mica.

Since such a variety of preparative procedures was employed, it is necessary to consider the extent to which sample preparation together with differences in imaging conditions might distort the resulting topographs. Both contact mode (*15, 34−37, 39*) and oscillating (noncontact or tapping) mode (*16, 19, 22*) were used in acquiring the AFM images of the ICM surfaces. While contact mode tends to provide superior resolution, in the tapping mode, the tip is in contact with the sample surface only at the end of a downward movement, minimizing possible lateral polypeptide deformations. Nevertheless, the overall coherence of molecular surface architecture revealed by these different approaches, together with the internal symmetry of the observed objects, argues against major distortions by the measurement systems. More difficult to address is the potential reorganization of components that could be driven by fixing to the mica surface or by detergent pretreatment (*16*) and membrane fusion (*34, 35*), but the observation of a similar overall organization in such membranes when attached directly to mica (*36*) and those supported by another membrane (*39*) suggests that no major reorganization was induced by adhesion to the support. It is harder to assess the effects of detergent treatment or flattening of the membrane. However, the degree of organization of photosynthetic complexes encountered in the AFM topographs of the *Rba. sphaeroides* membrane patches, in which the light-harvesting capacity and the ability of excitations to find an open RC phototrap are optimized (*16*) (see below), makes it unlikely that this has resulted from reorganization during treatment with subsolubilizing amounts of detergent but instead represents the native organization of the photosynthetic apparatus. Nevertheless, LH2 complexes are displaced vertically when natively curved wild-type and LH2-only membranes of *Rba. sphaeroides* adsorb onto a planar mica surface; this reorganization process appears to be driven by internal lateral pressure as the curved membrane adheres to the mica and leads to zigzag lines of raised LH2 complexes observed in AFM topographs (see Figure 7 below). The zigzag patterns were also observed for membrane fragments prepared in the absence of detergent (*22*). The more random arrangement encountered for *Rba. blastiucus* (*34*) is similar to that of other LH2-containing strains such as *Rsp.*

photometricum (*36, 39*) and *Phs. molischianum* (*15*), suggesting that the native architecture is also maintained despite freeze−thaw fusion procedures used to obtain satisfactory samples for AFM analysis. These various considerations are discussed in greater detail in the review by Scheuring et al. (*1*).

Membranes with Organized Arrangements of Photosynthetic Complexes. (i) Blc. viridis. In addition to serving as the source of the RC complex which provided the first atomic-resolution structure of an integral membrane protein by X-ray crystallography (*23*), *Blc. viridis* was also the earliest purple bacterium in which the supramolecular organization of photosynthetic complexes was assessed by TEM (*5−7*). *Blc. viridis* lacks the LH2 complex and contains a paracrystalline photosynthetic membrane, consisting of RC-LH1 core complexes arranged in a 2D hexagonal lattice (Figure 1). The low resolution of the projection maps of isolated membrane sheets, a result of inherently poor crystalline ordering, was insufficient for the assignment of the subunit architecture, which was still the case in the more recent analysis of 2D crystals of detergent-solubilized core complexes reconstituted with phospholipids (*41*). The native, highly organized arrangement and subunit structure of these core complexes only became apparent after high-resolution AFM surface views were obtained on fused *Blc. viridis* membranes (*35*) (Figure 1).

Through the application of increased loading forces to the AFM stylus by repeated high-magnification imaging, it was possible to nanodissect the bound tetraheme cytochrome (cytochrome c_{552}/c_{558}, the immediate reductant for the photooxidized RC-BChl *b* special pair), which strongly protrudes into the periplasm, thereby presenting an unobstructed periplasmic surface view of the spatial arrangement of the underlying RC-LH1 core particles in their native environment. This revealed the highly organized surface structure of hexagonally arrayed pseudocrystalline LH1-RC core complexes, consisting of single RCs surrounded by a closed ellipsoid of 16 LH1 $\alpha\beta$-heterodimers. The RC-L and RC-M subunits assumed a preferred asymmetric topography with a fixed distance distribution from the short ellipsis axis of the LH1 complex; this distance distribution reflects strong and specific associations within the RC-LH1 core that may represent important energy transfer constraints. Upon removal of the RC by nanodissection in some of the exposed core complexes, the LH1 complex rearranged into a circular structure, and it was proposed that this flexible behavior could promote breathing motions that would serve to facilitate passage of menaquinone/menaquinol through the normally closed LH1 structure (*35*) (see below). Importantly, thickness measurements of the membrane when tightly adsorbed to the mica surface, which gave a value of ≈124 Å, agreed closely with measurements made from the periplasmic to the cytoplasmic surface of the *Blc. viridis* RC in the crystal structure (*23*). The globular structure of the tetraheme cytochrome in the AFM images protruded ∼48 Å from the membrane plane, while for the RC-LH1 cores and the empty LH1 rings arising from nanodissection, values of ∼15 and ∼7 Å, respectively, were found.

(ii) Rba. sphaeroides Wild Type. While it has been noted that the highly organized and structurally identical packing of RC-LH1 core complexes in *Blc. viridis* may reflect the absence of intercalating LH2 complexes (*1*), AFM topographs of native photosynthetic membranes from the LH2-
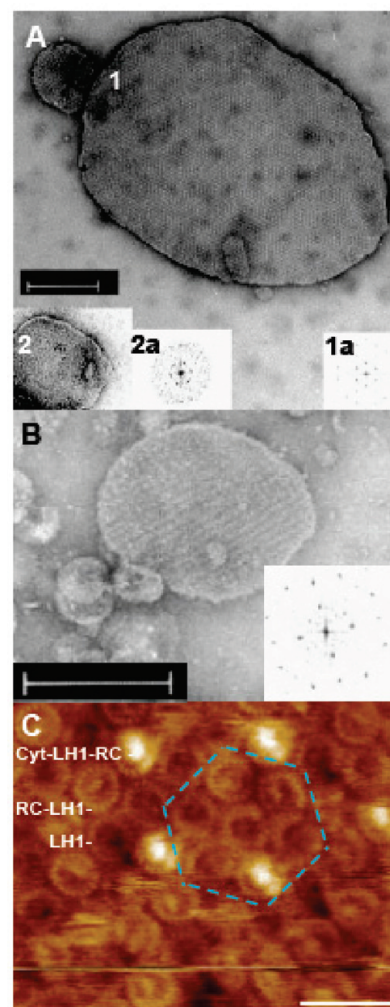

FIGURE 1: TEM and AFM analyses of *Blc. viridis* membranes. (A) TEM image of negatively stained membrane sheets (*40*) from light-grown (1) and dark heterotrophically grown (2) strain RA3, which is capable of expressing the photosynthetic apparatus in the dark. Fourier transform insets show hexagonal diffraction patterns of light-grown (1a) and dark-grown (2a) membranes. The scale bar is 200 nm. (B) TEM image of negatively stained smaller membrane fragments (*40*) from the dark grown *Blc. viridis* LH1-RC-H mutant, lacking the RC-L and RC-M subunits; a random distribution of disordered rows of RC-less core complexes predominated. The Fourier transform inset shows the frequently observed, square diffraction pattern of the altered membranes, resulting from the absence of the RC-L and RC-M subunits. The scale bar is 200 nm. (C) High-resolution AFM topograph of native membrane preparation subjected to freeze−thaw induced fusion (*35*). Samples were adsorbed onto mica surfaces in adsorption buffer and scanned in contact mode in electrostatically balanced imaging buffer at initial loading forces of ∼100 pN. Hexagonally packed protein complexes are distributed into three classes after nanodissection by applying increased loading forces to the AFM tip: Cyt-RC-LH1, tetraheme cytochrome $c_{552}/c_{558(1)}$−RC (L,M,H)$_{(1)}$−LH1 $(\alpha\beta)_{16}$; RC-LH1, RC (L,M,H)$_{(1)}$−LH1 $(\alpha\beta)_{16}$; LH1, LH1 $(\alpha\beta)_{16}$. Dashed blue lines indicate hexagonal packing, despite a lack of specific rotational orientation. The scale bar is 20 nm. Panels A and B reproduced from Figures 5 and 6, respectively, of ref *40*. Copyright 2003 Springer. With kind permission of Springer Science and Business Media. Panel C reproduced with permission from ref *35*. Copyright 2003 National Academy of Sciences of the United States of America.

containing purple bacterium *Rba. sphaeroides* have revealed a surprisingly ordered, interconnected network of both LH2 and dimeric RC-LH1 core complexes as well as ordered LH2-only domains (*16*) (Figure 2). Examination of the native
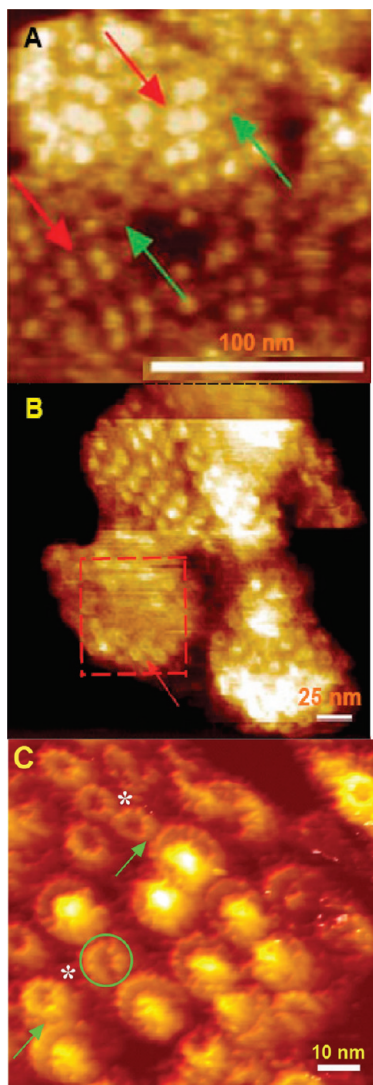
FIGURE 2: AFM analysis of native *Rba. sphaeroides* ICM (*16*). AFM topographs were obtained in oscillating mode in imaging buffer; resolution was maximized with a free tapping amplitude of 1−2 nm and setpoint adjusted to minimal forces. (A) View of membrane patches showing LH2 complexes (green arrows) interspersed between RC-LH1 core complexes (red arrows), consisting mainly of ordered, linear dimeric arrays arranged in rows; the central protruding feature within the RC-LH1 cores corresponds to the major portion of the RC-H subunit, indicating that the cytoplasmic face of the ICM is exposed. The *z* range = 6 nm (from darkest to lightest). (B) View of membrane patches showing two types of arrangements of photosynthetic complexes. The dashed red box demarcates a membrane patch consisting of LH2 complexes clustered together at different levels, which form an LH2-only domain lacking the RC-LH1 core complexes; the red arrow denotes the typical LH2 ring within the LH2-only domain. RC-LH1 core complexes predominate in the other patches; the size of each membrane patch approximates the surface area of an open ICM vesicle (chromatophore). (C) Three-dimensional representation of a small region of the membrane showing the mainly RC-LH1 core complexes and associated LH2 rings. Green arrows indicate contact points for energy transfer between LH2 and core complexes; asterisks denote LH2 rings in which a nine-unit structure is visible, while the green circle shows the LH2 complex sandwiched between two core complexes. On average, the LH1 complex protrudes above the lipid bilayer by ∼14 Å with a vertical tilt of 4.8° toward the monomer−monomer interface; LH2 protruded by ∼15 Å and had a tilt of 3.8°, while for the RC-H subunit, the average height above the bilayer was 37 Å. Reproduced from ref *16*. Copyright 2004 Nature Publishing Group.

surface architecture of the well-characterized ICM of *Rba. sphaeroides* was of considerable importance, since this highly studied purple bacterium provides a unique combination of accessible molecular genetics with an ICM that is amenable to an unparalleled variety of biochemical, spectroscopic, and ultrastructural probes. Accordingly, this facultative photoheterotroph has served as an ideal model organism for understanding the pimary light reactions of photosynthesis, as well as the regulatory mechanisms that control the levels of the participating protein complexes.

AFM images of membrane patches derived from chromatophores of *Rba. sphaeroides* revealed a unique organization of ICM domains as well as critical new features of the relative positions and functional associations of LH complexes (*16*). The dimeric RC-LH1 core complexes formed linear arrays that consisted of pairs of elliptical structures with protruding protein at their center (Figures 2A, red arrows). These arrays were interconnected by light-capturing domains of small LH2 rings (∼7 nm diameter), lacking a central density (Figures 2A, green arrows), also arranged in rows. Separate, specialized domains made up exclusively of LH2 complexes, some extending over an entire membrane patch, were also observed (Figure 2B, boxed area); these regions apparently represent the light-responsive complement of LH2, assembled during chromatic adaptation to low-intensity illumination (*42*) (see below).

What are the functional consequences of these ordered arrangements of photosynthetic complexes? The observed physical continuity between individual LH2 complexes, together with the contacts between LH2 and RC-LH1 core dimers (Figure 2C, interpreted further in the modeled region shown in Figure 3A), assures that excitations collected by any of the LH2 complexes are efficiently transferred to LH1, and subsequently to the RC, where a stable charge separation across the membrane is initiated. The LH1 complex is ideally positioned to serve as a hub for the collection of excitations obtained from LH2, which are then rapidly transferred to the RC. LH2 complexes situated between rows of RC-LH1 dimers form an essentially stable complement of pigment−protein complexes that fulfill the basic requirement for efficient trapping and transmission of light energy. Moreover, the occurrence of most of the RC-LH1 core complexes in dimeric associations, arranged in rows of up to six dimers (Figure 3A), means that an LH1 excitation can migrate along a series of dimers until an "open" RC is found.

These functional considerations are born out by the recent modeling of the structure and function of the *Rba. sphaeroides* chromatophore (*20, 21*), representing the first atomic-resolution, in silico structural depiction of proteins at the surface of a biological membrane vesicle (Figure 3B,C). The fidelity of this ICM vesicle reconstruction was tested through simulations of excitation migration over the modeled pigment network (*20*). Excitations were localized within individual BChl clusters to account for their strong couplings between the neighboring pigments of the B850 BChl rings of LH2 and the B875 BChl ellipses of LH1. Calculated excitation transfer times gave values of <1 ps for excitation flow from the B800 to the B850 LH2 ring and ∼10 ps for flow to a second B850 ring or to the S-shaped LH1-B875 BChl assembly, while 20 ps was calculated for the flow of excitations from B875 BChl to the RC; these values were distance-dependent and are similar to those measured by
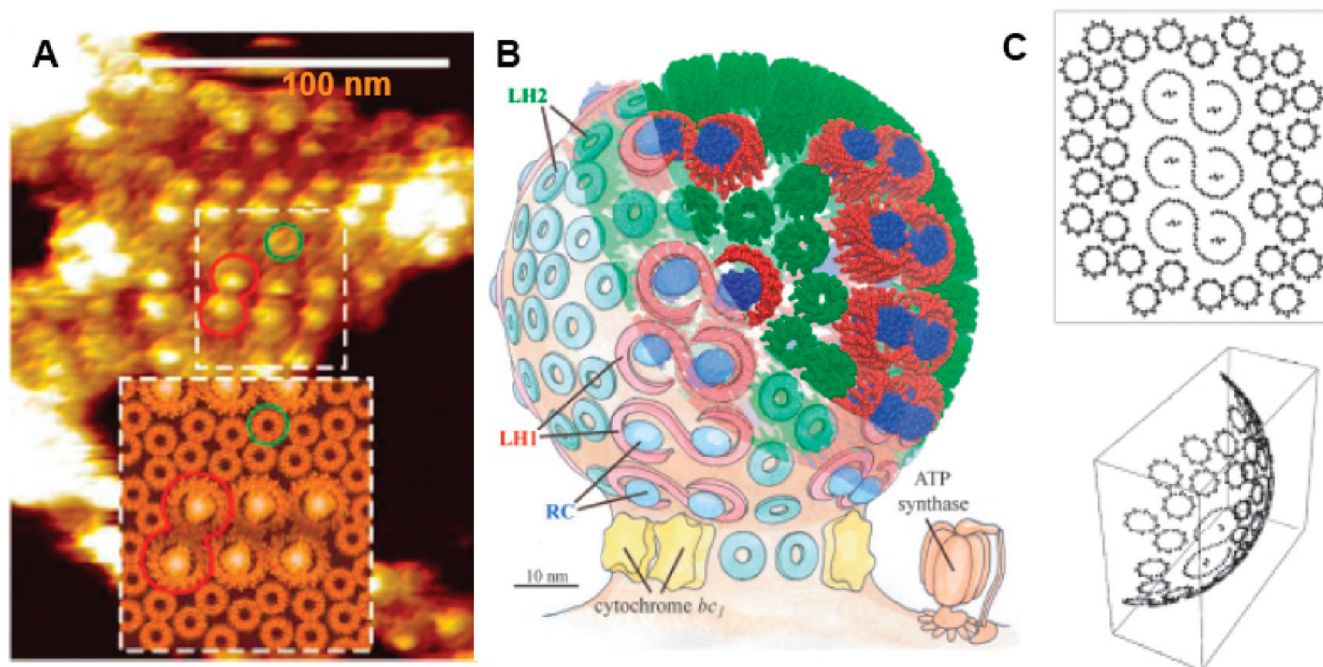
FIGURE 3: Molecular models deduced from AFM topographs of *Rba. sphaeroides* ICM. (A) Local arrangement of photosynthetic complexes in the ICM patch showing highly ordered linear arrays of the RC-LH1 core complex surrounded by LH2 complexes. For the bottom inset, existing structural data (*12, 24, 25*) were used to model the region denoted by the central dashed box; a typical RC-LH1 dimer is outlined in both images in a red outline and a representative LH2 complex by a green circle. See the text for details on how energy transfer efficiency is maximized in this arrangement of photosynthetic complexes. (B) Overall structural and functional depiction of the cytoplasmic aspect of a *Rba. sphaeroides* ICM vesicle with an inner diameter of 60 nm (*20, 21*). The model is based upon AFM (*16*) and LD (*18*) data and illustrates the long-range organization of photosynthetic complexes over the surface of a vesicle. The protein surfaces are modeled to atomic resolution at the top right, on the basis of the projection map of the dimeric RC-LH1 core structure (*49*) and the X-ray structure of the nonameric LH2 complex from *Rps. acidophila* (*51*). Dimeric cytochrome bc_1 complexes are portrayed schematically at the vesicle neck, with an ATP synthase located in the CM. The planar ICM patch modeled here is the same as that shown in panel A, turned clockwise by 90°. (C) An area-preserving map was constructed by projecting from the planar surface of the AFM topograph (top) to the native spherical shape of an ICM vesicle (bottom), to correct for the flattening of membrane patches on the mica support. An inverse projection was used in the positioning of the pigment−protein complexes at the vesicle surface (*20*). Panel A reproduced from ref *16*. Copyright 2004 Nature Publishing Group. Panels B and C reproduced from ref *20*. Copyright 2007 National Academy of Sciences of the United States of America.

time-resolved excitation dynamics (*43*). A plausible average excitation lifetime of 50 ps was computed across the overall vesicular structure, which corresponds to a quantum yield of 95%. This indicated that all pigment clusters are functionally connected, such that the modeled vesicle (Figure 3B) comprises an efficient network for energy transfer.

The RC-LH1 dimer arrangement in rows separated by linear clusters of LH2 explains why mutant cells lacking LH2 form elongated tubular membranes (*44, 45*). Because of the absence of LH2 separating the RC-LH1 complexes, these mutants display a striking pattern of closely packed, highly ordered rows of dimeric RC-LH1 particles arrayed helically along the entire tubule length (*32, 46*). Their structure was further refined by image analysis of negatively stained tubule preparations, in which the particles appeared as open S-shaped assemblies of dimeric core complexes (*32, 47*).

Even in high-resolution AFM topographs of the dimeric cores (Figure 2C), it was not possible to confirm whether the LH1 annuli were incomplete, due to the decreased resolution at the junction between the two halves of the in situ core structure (Figures 2C and 3A). The open nature of the LH1 ellipses, as well as the apparent positions for the core organizing PufX polypeptides, has been resolved in an 8.5 Å projection structure (*48, 49*) arising from a cryo-EM analysis of 2D crystals of the *Rba. sphaeroides* RC-LH1−PufX dimer, together with a more recent three-

dimensional (3D) reconstruction derived from single-particle analysis of negatively stained dimers at cryogenic temperatures (*50*) (Figure 4). In the EM projection map (Figure 4A), transmembrane helices are clearly visualized, permitting localization of all helices associated with the LH1 and RC complexes, as well as assignments for positioning of the two PufX helices (green circles).[2]

(iii) Rba. sphaeroides Mutant Strains. PufX is required for the dimerization of the RC-LH1 complex (*32, 58, 59*), and mutants in the *pufX* gene have a photosynthesis-negative phenotype (*60, 61*), attributed to defects in the movement of UQ redox species to and from the RC (*52*). Remarkably,

---

[2] An alternative model, based upon an EM projection map obtained with 2D crystals of the *Rba. sphaeroides* core dimer at 26 Å resolution (*52*), places two PufX polypeptides within the LH1 annulus, in contact at the junction between the two halves of the dimeric S-shaped structure consisting of 24 LH1 αβ subunits, compared to 28 in the 8.5 Å structure (*49*). However, localization of PufX near the RC Q_B site in this PufX−PufX helix−helix model would require rotation of the RC within the dimer structure to a point where it no longer fits with the known EM density (*49*) or with the Q_Y transition moment orientation of the RC special pair as determined by LD of native dimeric complexes in tubular membranes (*17*), and verified in EMs of these preparations after negative staining (*32*). In addition, the position of the PufX helices in the 8.5 Å structure (*49*) closely resembles the location of the W helix, an apparent PufX homologue, in the monomeric RC-LH1 core X-ray structure of *Rps. palustris* (*25*). Clearly, more precise structural data will be necessary to resolve this impasse.
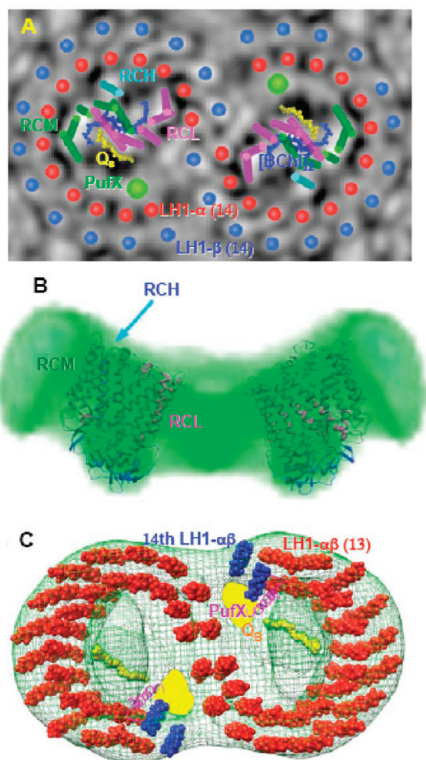
FIGURE 4: Structural models of the *Rba. sphaeroides* RC-LH1 dimer. (A) Schematic representation of the projection structure at 8.5 Å resolution from cryo-EM analysis of tubular 2D crystals, as viewed from the cytoplasmic aspect of the complex (*49*) as in AFM topographs (*16*). The α-helical positions are coded in their respective identifying colors and are superimposed upon a contour map of averaged gray level representation of projection densities in tubular 2D crystals, with black denoting areas of lowest density. The green circles indicate the putative locations of the two PufX transmembrane helices; the densities in these region fall outside the RC envelopes and have magnitudes and shapes similar to those of the stronger RC and LH1 helical densities, and each green circle is in a position analogous to that of helix W, an apparent PufX structural homologue, modeled in the crystal structure of the *Rps. palustris* monomeric RC-LH1 complex (*25*). As expected from interaction studies (*53*), the PufX location is closest to the LH1 α-subunits; it is also adjacent to the RC Q_B sites and the widest distances between LH1 α-subunits, consistent with a structural role for PufX in assuring that a portal exists for the flow of Q redox species to and from the RC (*54*). (B) 3D reconstruction of the RC-LH1 dimeric complex calculated from TEM analysis of negatively stained single particles (*50*). A side view of the semitransparent 3D reconstituted dimer model is colored green with atomic structures of the *Rba. sphaeroides* RC inserted; their orientations were fitted as described in ref *50*. The individual monomers are inclined toward each other on the periplasmic aspect of the complex, resulting in a V-shaped structure, as demonstrated in this depiction of the surface. (C) 3D model of the RC-LH1 dimer (*48, 50*) viewed from the cytoplasmic side as in AFM topographs (*16*), showing the transmembrane helices of the LH1 complex (space-filling representations) in red with the fourteenth αβ-pair colored blue and the transmembrane domain of the PufX polypeptide (magenta ribbons) taken from the recently published NMR structure (*55*). LH1 αβ-pairs are fitted into the tilted 3D dimer structure deduced from single-particle analysis (green mesh) using coordinates from ref *25* and further adjusted according to the cryo-EM projection map (*49*). Only the Q_B component of the RC is shown (yellow, space-filling representation); the space adjacent to the fourteenth LH1 αβ-pair, highlighted in yellow, represents a cavity that is thought to accommodate a quinone pool (*56, 57*). Panel A reproduced from ref *49*. Copyright 2005 Elsevier. Panels B and C reproduced from ref *50*. Copyright 2008 The American Society For Biochemistry and Molecular Biology.

LD measurements with oriented membranes (*17, 18*), together with the local organization of photosynthetic complexes as visualized by TEM (*32*) and AFM (*16*), have demonstrated that PufX also confers a long-range order upon the core structures in the tubular membranes of *Rba. sphaeroides* mutants lacking LH2 (*17*), as well as in the spherical ICM continuum found in the wild type (*18*) (for a recent comprehensive review on PufX, including different models for the positioning of PufX in the RC-LH1 structure, see ref *62*). The difference in absorption between horizontally and vertically polarized light as measured by LD has permitted the comparison (*18*) of the transition dipole moment orientations of the BChl chromophores of the LH2 (*51*), LH1 (*25*), and RC (*63*) complexes in intact, oriented membranes in the wild type with those of mutants lacking PufX, as well as strains lacking LH2, with and without PufX (*17−19*). In this manner, light-minus-dark LD measurements employing laser flashes in the millisecond range, after overlapping changes in the LH complexes are complete, showed that PufX induces a nonrandom orientation on the RC within the LH1 ring, as well as the alignment of all RC-LH1 cores in regular arrays. This effect was found in both the RC accessory BChl and the BChl special pair signals, but unlike the LH2⁻PufX⁻ membranes, in which a random order of the RC-BChl chromophores was found (*17*), the flash-induced light-minus-dark LD changes in the PufX⁻LH2⁺ strain suggested that as a result of the presence of the LH2 complex, a partial ordering in the RC-LH1 packing lattices is maintained (*19*).

Figure 5 presents the results of an AFM analysis of membrane patches from the PufX⁻ mutant, together with the proposed packing lattices in membranes from strains containing the RC-LH1 core complex with and without the LH2 complex and PufX (*19*). The unusual LD signal caused by the absence of PufX in an otherwise wild-type background was further investigated by an AFM analysis of adhered membranes. As seen in Figure 5A, the absence of PufX has led to a complete reorganization of the membrane, such that extensive, ordered arrays of monomeric core complexes, showing the protruding portion of the RC-H subunit, form domains from which the LH2 complex is largely excluded and is instead segregated to the more curved membrane domains (*18*). Semihexagonal arrangements of loosely (Figure 5B) and tightly (Figure 5C) packed RC-LH1 monomers are seen in these higher-resolution AFM topographs, where randomly oriented RCs are also visible in interiors of the former and uniformly oriented RCs are present in the latter (*19*).

Accordingly, the core and LH2 complexes are assembled in a variety of packing lattices, depending upon the combination of the LH2 complex and PufX polypeptide present in the various mutant strains (*17−19*). Uniformly oriented dimeric core complexes, as suggested from the light-minus-dark LD spectra of the RC-BChl LD signals, are shown for the dimeric RC-LH1 complexes present in the tubules of the LH2⁻ strain, and in the vesicular ICM of the wild type (Figure 5D,F). In contrast, hexagonal packing lattices of randomly arranged monomeric RC-LH1 cores are present in the LH2⁻PufX⁻ and PufX⁻ mutants (Figure 5E,G), with a second group of uniformly oriented core monomers in the strain lacking PufX (bottom lattice in Figure 5G), where the momomeric core domains coexist with curved LH2 domains.
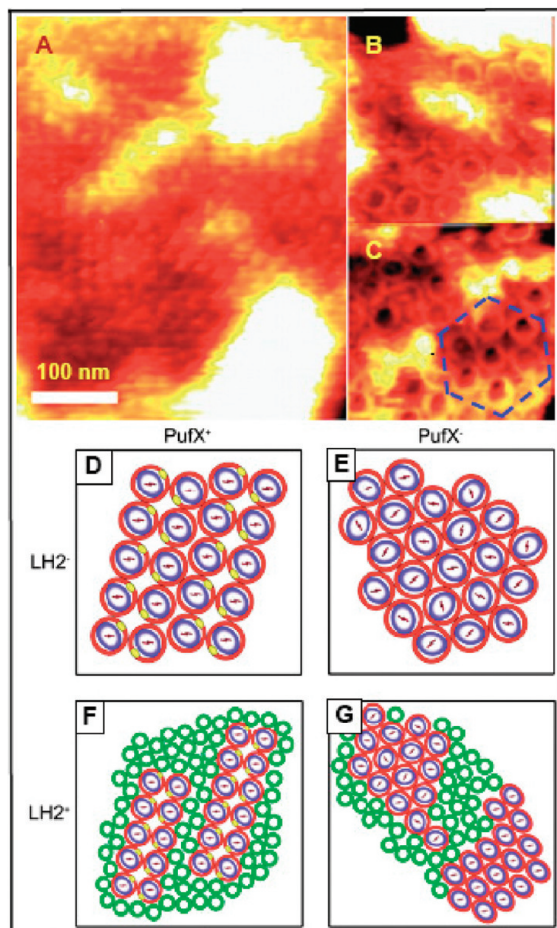
FIGURE 5: AFM analysis of monomeric RC-LH1 complexes in ICM from the *Rba. sphaeroides* strain lacking the PufX polypeptide and models of packing lattices of photosynthetic complexes in membranes containing RC-LH1 core complexes with and without the LH2 complex and PufX (*19*). The PufX⁻ strains were grown under low aeration in the dark, and photosynthetic membrane preparations arising from the gratuitously formed ICM structures were subjected to tapping mode AFM as described in the legend of Figure 2. (A–C) AFM analyses of the PufX⁻ strain. (A) Enhanced AFM topograph of the cytoplasmic aspect of the membrane patch, showing the protruding portion of the H subunit of the RC in a domain consisting largely of monomeric RC-LH1 complexes. (B and C) High-resolution AFM topographs of periplasmic aspects of membrane patches showing portions of domains consisting largely of monomeric RC-LH1 complexes, 3D enhanced for clarity. (D–G) Schematic representations of four different packing lattices of photosynthetic complexes. RC-LH1 complexes are depicted as red circles representing LH1, surrounding RCs demarcated as blue ovals with bars inside showing the Q_Y transition orientations of the RC-BChl special pair, and PufX polypeptides as yellow ovals; LH2 is depicted as green circles. (D) Packing lattice in tubular membranes from the LH2⁻ strain, containing tightly packed rows of dimeric RC-LH1 complexes, as deduced from LD (*17*) and TEM analysis of negatively stained preparations (*32*). (E) Packing lattice in crystalline membrane sheets from the LH2⁻PufX⁻ strain, with pseudohexagonally packed monomeric RC-LH1 complexes, as deduced from LD (*17*) and TEM analysis of negatively stained preparations (*32*). (F) Packing lattice in wild-type ICM, as deduced from AFM (*16*) and LD (*18*) analyses of membrane patches and chromatophores. The ICM retains the uniformly oriented rows of dimeric RC-LH1 complexes, despite the presence of LH2 arranged in the two types of domains observed by AFM (*16*). (G) Packing lattices in membranes of the PufX⁻ strain, deduced from AFM (panels A–C) and LD analyses (*19*). The top and bottom packing lattices represent randomly and uniformly oriented RC-LH1 core complexes, respectively. Reproduced from ref *19*. Copyright 2008 Biophysical Society.

Thus, the absence of PufX also prevents the interconnection of the arrays of RC-LH1 core complexes by interspersed rows of LH2 complexes (compare panels F and G of Figure 5).

Taken together, these LD (*17–19*), AFM (*16, 19*), and ultrastructural (*32*) results demonstrate that the appearance of distinct membrane protein domains and the associated membrane curvature are retained even in strains lacking PufX, resulting in conversion of the RC-LH1 complex from a dimeric form to a monomeric form. This implies that the generation of membrane organization and shape does not require specific protein–protein interactions between complexes but is instead governed by a general mechanism involving depletion-induced attraction and macromolecular crowding, as specified by colloid theory (*64*). In this proposal, which represents the development of a dynamic membrane model derived from Monte Carlo simulations, ICM domain formation and invagination are driven by the crowding and geometry of the core and LH2 complexes, as well as curvature mismatch between the interacting faces of adjacent complexes, due to asymmetries in size and shape (*19*). The strikingly "bent" conformation of the core dimer (Figure 4B,C) may serve as a major driving force in the formation of budded, near-spherical intracytoplasmic membranes in *Rba. sphaeroides*, although LH2 complexes must also contribute to their overall shape, because spherical membranes are also formed with LH2 as the only photosynthetic complex (*44, 45*). ICM curvature is further augmented by the insertion of additional LH2 during chromatic adaptation to lowered light intensity (*42, 65*), which is able to assemble into extensive LH2-only domains (Figure 2B) (*16*). Packing forces resulting in heterogeneous RC-LH1 core-LH2 mixtures and ultimately in the formation of paracrystalline LH2 domains may be responsible for exclusion of ATP synthase and the cytochrome bc_1 complex and their apparent positioning in nonpigmented regions as proposed in refs *20* and *21*. Recent large-scale molecular dynamics simulations at atomic resolution indicate that the bc_1 complex has some preference for positively curved bilayers and may rely on such a shape to assume its optimal location. These in silico studies also confirmed the protein-induced shaping and dynamic membrane curvature inducing properties of both LH2 arrays and the bent dimeric RC-LH1–PufX complex (*66*). Moreover, site-directed mutagenesis has also suggested a role for interaction with the surrounding lipid molecules and the carotenoid polar headgroup in shaping the properties of the LH2 complex (*67*).

Since the well-characterized LH2 complex provides a valuable model for understanding the packing properties of an integral membrane protein in a native curved membrane environment, a strain of *Rba. sphaeroides* with LH2 as the sole pigment–protein complex was constructed to eliminate the effects exerted by the rows of RC-LH1 core complexes on LH2 domain organization (*22*). After cell disruption, the ICM of this LH2-only strain gave rise to spherical ICM vesicles ~53 nm in diameter, which after mild detergent treatment (*16*), gave rise to membrane patches that adsorbed onto mica surfaces in the form of opened flat sheets of ≤120 nm, amenable to imaging by tapping mode AFM (Figure 6). The LH2 complexes within the flat membrane sheets exhibited a regular corrugated appearance (Figures 6A), arising from the deformation of curved membrane fragments during the adsorption process, such that approximately half
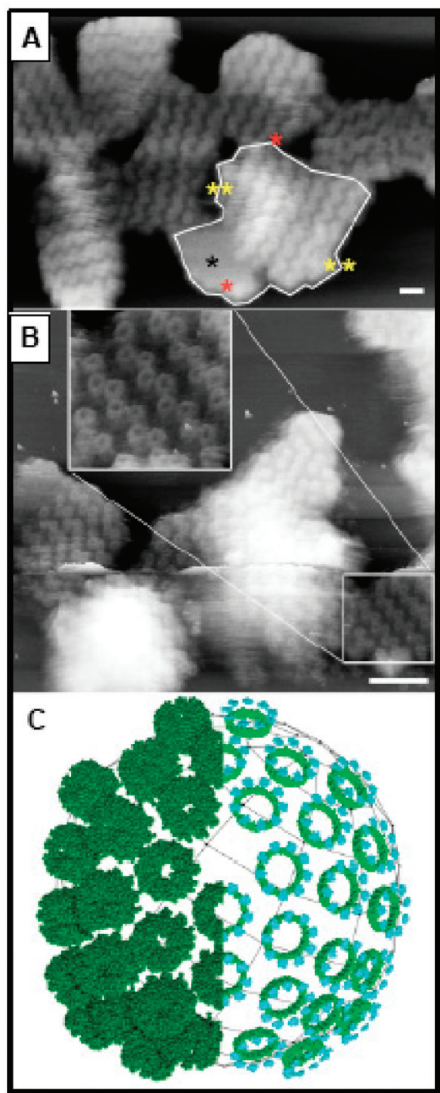
FIGURE 6: AFM analysis of native ICM from RC-LH1⁻ *Rba. sphaeroides* strain DPF2G (*22*), using a standard tapping mode liquid cell essentially as described in the legend of Figure 2. (A) 3D representations of a group of isolated ICM patches exhibiting distinct orientations of highly regular zigzag lines, used in demarcating entire flattened vesicles. An entire flattened ICM vesicle is outlined with possible zones of contact in the original spherical structure designated by the respective yellow and red asterisks. The black asterisk denotes an area of protein-free lipid bilayer, similar to that observed in the AFM analysis of the *Rps. palustris* ICM (*37*) (see below). The scale bar is 20 nm; full gray scale 15 nm. (B) 3D representations showing regions of well-ordered and well-defined dimeric LH2 complexes used in measurements of both intracomplex and intercomplex center-to-center distances (7.7 ± 0.5 and 9.2 ± 0.4 nm, respectively), and the angle which they subtend (112.1 ± 7.0°). The inset shows an enlargement of a highly ordered area demarcated by the white box. Areas of more disordered LH2 complexes that do not form a regular zigzag arrangement are also evident. The scale bar is 20 nm; full gray scale 20 nm. (C) Model showing the packing of LH2 complexes as suggested from AFM analysis. Space-filling representations of the LH2 complex (*51*) (left half) were placed on the surface of a sphere 50 nm in diameter using the average center−center separation of 8.5 nm in a predominantly hexagonal organization, resulting in an overall pattern resembling that of an icosahedral viral capsid. The right half depicts the arrangement of only the B800 (light blue) and B850 (green) BChl macrocycles in which hexagonal arrays of LH2 complexes are more obvious. The predicted distance between the closest B850 BChls is 3.8 nm. Reproduced from ref *22*. Copyright 2008 The American Society For Biochemistry and Molecular Biology.

of the complexes are translated upward by ∼1 nm, relative to the remaining complexes which adhere to the mica by electrostatic attractions. An equal distribution of lateral forces over the entire adsorbed membrane results in a consistent height displacement between the upper and lower zigzag lines for all the LH2 complexes within mutant chromatophore patches (Figure 7A).

Measurements of the distances between well-defined LH2 complexes and the angles between their tilted dimeric pairs (Figure 6B) showed that complexes within a pair are closer together than they are to adjacent complexes, reflecting protein−protein contacts between the LH2 complexes within a dimer and the presence of lipid between the adjacent dimeric complexes. These data formed the basis for the modeling of LH2 organization in the native curved ICM (Figure 6C), in arrays where the closest distances between B850 BChls of 3.8 nm are able to account for the lifetime of ∼5 ps attributed to energy transfer between LH2 complexes in LH2-only membranes (*68*). Sufficient room is available for phospholipid molecules between the packed complexes, which would permit the diffusion of quinone redox species through the LH2-only domains in the native wild-type ICM. While this arrangement would provide conduits for the movement of electron carriers between the RC and a distantly located cytochrome bc_1 during cyclic electron flow in *Rba. sphaeroides*, it has been suggested that the LH2 complexes in *Phs. molischianum* exist in protein−protein contact in the LH2-only domains of this species, and others in which the ICM takes the form of flattened, thylakoid-like discs (*15*), as discussed below. Figure 7 shows that despite the superficially similar appearance of the zigzag lines in the native LH2-only membranes compared to those observed in 2D crystals of LH2 of *Rba. sphaeroides*, all the complexes are in the native orientation, whereas the packing in the crystal is an alternating up−down arrangement.

Membranes with More Random Arrangements of Photosynthetic Complexes. (i) Rsp. photometricum. Recent high-resolution AFM analyses of the ICM from a number of other purple bacteria have revealed less regular organizations of photosynthetic complexes compared to those observed in *Rba. sphaeroides*, with a considerable mixing of peripheral LH2 and RC-LH1 cores. This dense, partially ordered packing of complexes was first encountered in flat membrane fragments arising from the stacked ICM of *Rsp. photometricum* (*36, 39*) (Figure 8). Regions with a mixture of randomly organized, monomeric RC-LH1 core ellipses of 16 LH1 subunits and mainly nonameric LH2 rings predominated, with a respective proportion of ∼1:3.5 in membranes from cells grown at high light intensity (Figure 8A), albeit with considerable intercomplex clustering. These mixed regions coexisted with paracrystalline LH2 domains, where the additional peripheral LH2 antennae are packed during chromatic adaptation to lowered light intensity (Figure 8B). The existence of the photosynthetic complexes in tightly packed clusters under both high- and low-intensity illumination assures that individual antenna proteins do not segregate too far from the bulk of the light-harvesting system to function in the transfer of excitation energy to neighboring complexes. In some areas, core complexes are seen in contact (see especially Figure 8C); such connectivity increases the probability that excitons will find an open RC, enhancing rapid energy trapping as in the organized arrangement of
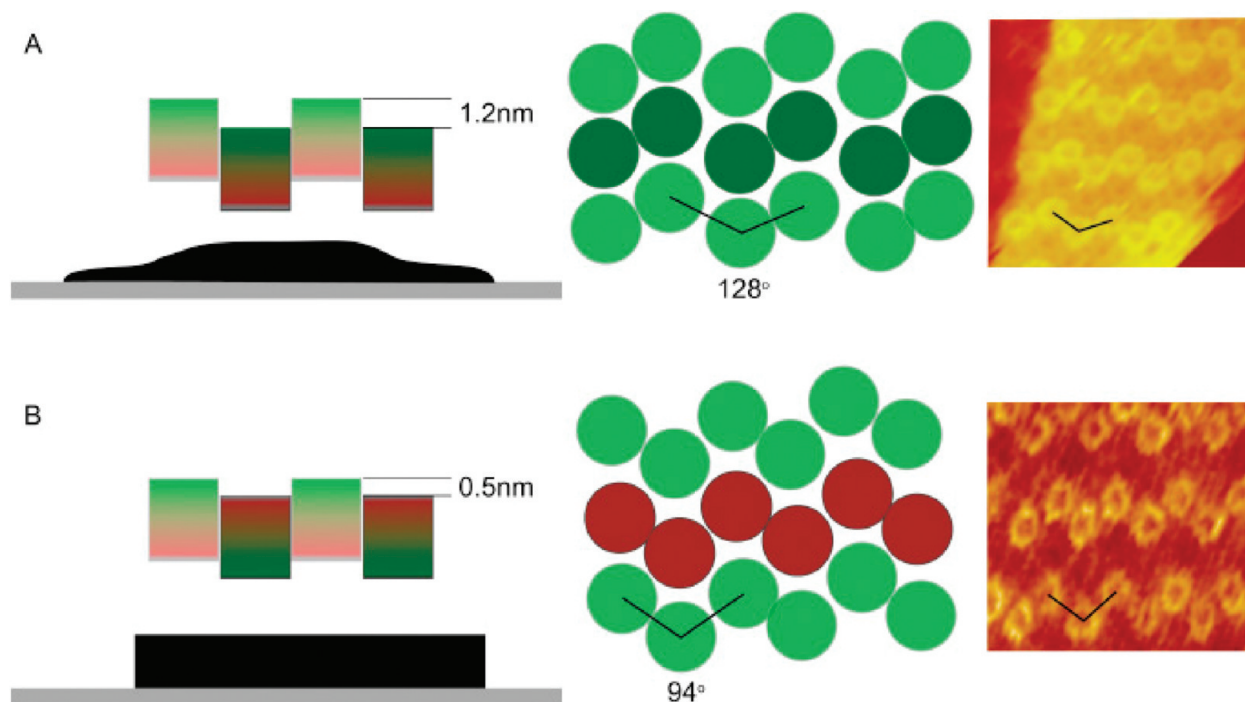
FIGURE 7: Comparison of the packing of LH2 complexes in the flattened native ICM of LH2-only *Rba. sphaeroides* strain DPF2G and in reconstituted 2D LH2 crystals. The complexes are depicted in cartoon form in side and top views, together with the relevant AFM height image. (A) Arrangement of the complexes in the membrane after flattening on mica. The complexes are all in the same orientation, the height difference being ∼1.2 nm and the angle subtended by three adjacent complexes being ∼128°. (B) Arrangement of the complexes in a 2D LH2 crystal on mica. The complexes are in alternating orientations, the height difference being ∼0.5 nm and the angle subtended by three adjacent complexes being ∼94°.

core complexes found in *Rba. sphaeroides* (*16*). It is also noteworthy that in the monomeric RC-LH1 core assemblies imaged in the native membrane, the RCs were randomly oriented within the closed LH1 ellipses (*1*), in contrast to the uniformly oriented long-range order observed for the dimeric RC-LH1 cores in wild-type *Rba. sphaeroides* (Figure 5F).

Surprisingly, a heterogeneous distribution of LH2 ring sizes was also found in *Rsp. photometricum* (*70*), in which the most abundant sizes ranged from octamers to decamers, with nonamers making up 70% of the total. This ring size heterogeneity represents a native feature of LH2 assembly and was accompanied by spectral heterogeneity, in which the near-IR absorption spectra of the smaller complexes are gradually blue-shifted relative to those of the larger complexes, as observed previously in bands of *Rba. sphaeroides* LH1 (*46*) and LH2 (*71*) complexes of various sizes, arising from dissociation during electrophoretic isolation. The natural variability in ring sizes could represent a strategy for generating broader absorption spectra to maximize the collection of near-IR radiation, as well as the optimization of photosynthetic complex packing in a heterogeneous membrane.

The high-resolution AFM topographs (lateral and vertical resolution of ∼10 and ∼1 Å, respectively) arising from the detailed studies of the *Rsp. photometricum* ICM (Figure 8D,F) have formed a basis for the docking of atomic structures into the tightly packed images of multiprotein assemblies of photosynthetic complexes (*14*). The docking of an atomic structure into an envelope of lower resolution requires knowledge of the translational and rotational degrees of freedom within the space occupied in this case by membrane proteins, which is restricted by the membrane

plane to the translational *X* and *Y* coordinates and the rotational angle around the perpendicular *Z* axis. The atomic-resolution structures (*11−13*) were fitted into the high-resolution AFM topographs of the *Rsp. photometricum* ICM (*14*), giving rise to a comprehensive molecular picture of the overall photosynthetic machinery.

By employing the spatial coordinates and rotational orientations into which these high-resolution crystallographic structures were rotationally docked, structural models of the supramolecular assemblies shown in panels E and G of Figure 8 have emerged (*14*), with a precision for atoms at complex interfaces and in the pigments estimated at ∼3 Å (*4*). For the ICM of cells adapted to high light intensities, a model was constructed in this manner which consists of an ensemble of seven nonameric LH2 complexes surrounding one core complex, made up of a closed elliptical assembly of 16 LH1 αβ-heterodimers, with a single RC in the interior (Figure 8E). This entire *Rsp. photometricum* assembly is organized to provide for efficient movement of excitons toward the central RC, while the opening in the ring of LH2 complexes, which is found when seven LH2 nonamers surround a core structure, effectively ensures that all LH2 complexes are in contact with one another on at least one side. Such a minimization of the spacings between complexes could conceivably enhance energy storage within any of the individual LH2 nonamers when the RC is closed and back transfer from LH1 to LH2 has occurred. Using the ICM of low-light cells (Figure 8F), an antenna domain of 15 tightly packed LH2 complexes was modeled (Figure 8G). The closely packed, rigid complexes within such *Rsp. photometricum* LH2-only domains apparently exclude quinone/quinol diffusion between them and are thus suggested to enhance
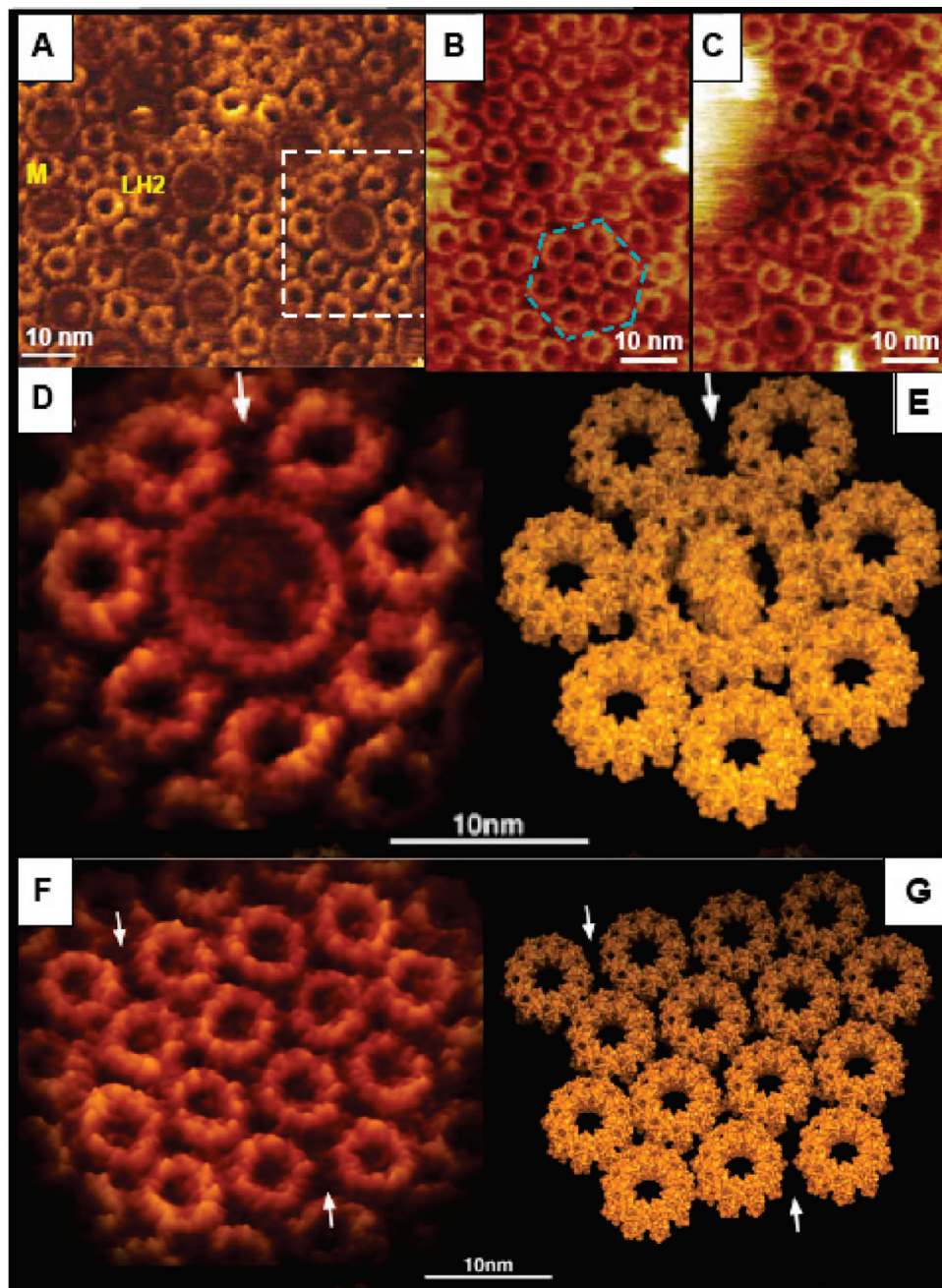
FIGURE 8: AFM analysis of native *Rsp. photometricum* ICM. AFM topographs were obtained in contact mode essentially as described in the legend of Figure 1. (A) High-resolution topograph of high-light-adapted ICM (*39*). M, closed monomeric RC-LH1 core complex; LH2, nonameric LH2 complex. The core complexes and LH2 rings are arranged randomly and are found in an ~1:3.5 ratio. (B and C) High-resolution topographs of low-light-adapted ICM. In panel B, an area of mixed core complexes and LH2 rings is shown, with an overall core complex:LH2 ratio of ~1:7; areas of paracrystalline hexagonal arrays of LH2 are also seen that are devoid of core complexes. In panel C, an area is seen that contains substantially more core complexes than the average. In these regions, as in panel A, several core complexes are found in contact, and the overall ~1:3.5 core complex:LH2 ratio is retained. (D and E) AFM topograph (D) (encompassing the dashed region in panel A) used as raw data for docking atomic-resolution structures (*11−13*), giving rise to the structural model of the supramolecular assembly of a core complex surrounded by LH2 (E) (*14*). A surface representation of the final structural model is shown; models showing only protein backbones and pigments alone in the foreground can be found in ref *14*. The RC-H subunit has been removed by nanodissection with the AFM tip in which loading forces were increased to 200 pN at scanning frequencies of 3000 nm/s. The arrow here and in panel E denotes a lipid bilayer space between LH2 complexes, which is thought to be functionally important in facilitating membrane mobility for quinone−quinol exchange to and from the core complex (*69*), just as the openings in the dimeric RC-LH1 complexes at the ends of linear core chains are thought to serve in this function in *Rba. sphaeroides* (*20*). (F and G) AFM topograph (F) (encompassing the region demarcated in panel B by the dashed hexagon surrounded by nine additional complete LH2 complexes) used as raw data for docking the atomic-resolution structure of LH2 (*12*), giving rise to the structural model of a supramolecular assembly of tightly packed LH2 complexes (G) (*14*). A surface representation of the final structural model is shown; models showing only protein backbones and pigments and pigments alone in the foreground can be found in ref *14*. Arrows in panels F and G denote weak distortions within the paracrystalline LH2 lattice, found only at edges of the antenna patches, while the rest of the LH2-only domain consists of tightly packed, rigid complexes. Average structure assemblies are depicted in panels E and G, as a consequence of the average crystallographic structures used in the docking (*14*), and no attempt was made to account for individual polypeptide chain fluctuations. Panels A−C reproduced from ref *39*. Copyright 2005 American Association for the Advancement of Science. Panels D−G reproduced from ref *14*. Copyright 2007 Elsevier.
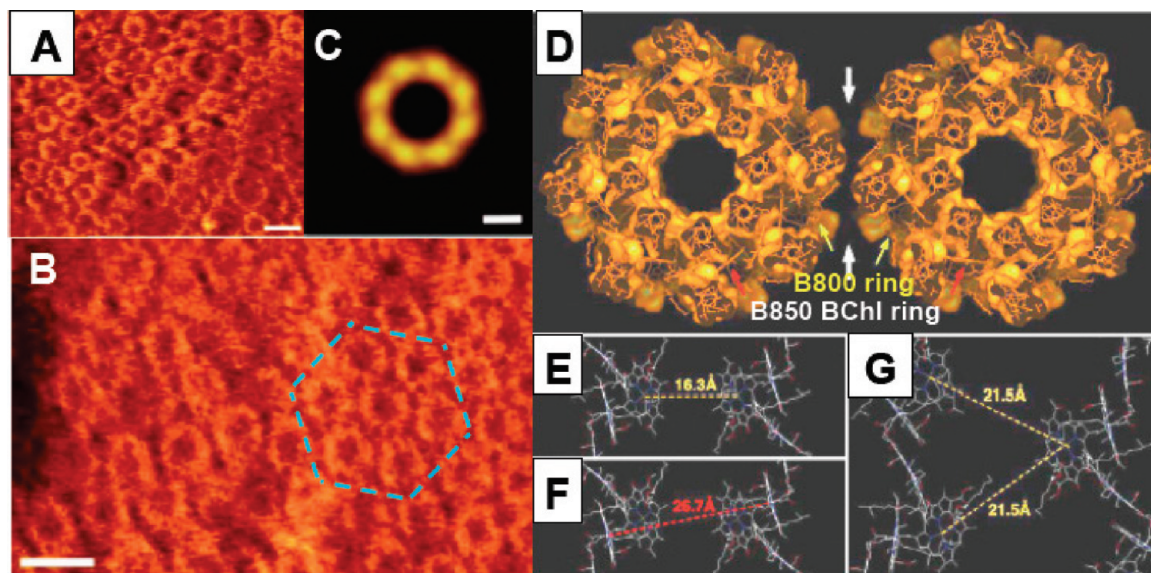
FIGURE 9: AFM analysis of native *Phs. molischianum* ICM (*15*). AFM topographs were obtained in contact mode essentially as described in the legend of Figure 1. (A) Topograph of the low-light-adapted ICM showing the region containing a mixture of LH2 and monomeric RC-LH1 core complexes. While a wide variety of complex assemblies was encountered, ∼70% of the core complexes were connected with another core, and the separate core complexes were most frequently surrounded by six or seven LH2 complexes. (B) Antenna domain consisting of hexagonal paracrystalline arrays of LH2, devoid of core complexes (color scale in panels A and B, 5 nm). (C) Eight-fold symmetrized LH2 average (color scale, 1 nm). The subunits reveal a slight left-handed twist. (D) Structure of adjacent LH2 rings sliced slightly above each B850 BChl ring in a molecular surface representation. Large white arrows denote the space limit between the two rings. (E−G) Intercomplex distances between BChls in adjacent LH2 complexes within LH2 domains varied, depending on the rotation of the LH2 ring: for B800 BChl → B800 BChl, they were as short as 16.3 Å (E), and for B850 BChl → B850 BChl, they ranged between 26.7 and 28.3 Å (F) and were as long as 21.5 Å for B800 BChl → B800 BChl (G). Reproduced from ref *15*. Copyright 2005 Elsevier.

channel diffusion between the RC and cytochrome bc_1 complex (*69*).

(ii) Phs. molischianum. The analysis of the *Phs. molischianum* ICM, which also consists of thylakoid-like structures suitable for contact mode AFM, has provided the basis for another important modeling effort. As seen in *Rsp. photometricum*, LH complexes are segregated into two structurally different types of domains, consisting of a mixture of core and octameric LH2 complexes, also in an approximate ratio of 1:3.5 (Figure 9A), and paracrystalline, hexagonally packed octameric LH2 rings (Figure 9B,C) (*15*). Since the structure of the *Phs. molischianum* LH2 ring has been determined to atomic resolution by X-ray crystallography (*13*), it was possible to model adjacent in situ LH2 complexes within LH2-only domains by using the atomic coordinates (Figure 9D). These values, together with the LH2−LH2 center-to-center distance of 74 Å measured in the AFM analysis, as well as the B800−B800 BChl and inter- and intradimeric B850 BChl distances determined in the crystal structure, were used to deduce the exact pigment distances between neighboring LH2 complexes for the first time within a membrane environment (Figure 9E−G). The intercomplex distances between central Mg^{2+} atoms calculated in this manner (16.3−28.3 Å) are all within the distance of ≤30 Å (*72*) that is necessary to ensure efficient B800 BChl → B800 BChl and B850 BChl → B850 BChl energy transfer between adjacent complexes. Because LH2 complexes with both 8- and 9-fold symmetries both form hexagonal packing lattices, their assembly is driven by high packing densities and solvation effects within these domains, rather than specific protein−protein interaction as dictated by their inherent symmetry differences. The mechanisms governing such packing effects have been recently developed in greater detail by Frese et al. (*19*), as discussed above.

(iii) Rps. palustris. The metabolically versatile purple bacterium *Rps. palustris* also gives rise to native chromatophores that are amenable to contact mode AFM analysis (*37*). These isolated membranes consist of membrane sheets arising from a complex ICM structure consisting of infoldings of the CM that take the form of regular bundles of stacked, flattened thylakoid-like membrane sacs (Figure 10A) (*38*). Indeed, the wide variety of LH2 and RC-LH1 core complex organizations and domain arrangements revealed by AFM (Figure 10B−E) reflects this complexity of CM/ICM organization into stacked and unstacked lamellar regions. In low-light cells, randomly arranged mixed domains (Figure 10B) coexist with hexagonally packed LH2 areas (Figure 10C), as seen in other purple bacteria with lamellar ICM structures. It is possible that the mixed domains arise largely from the proximal layers within the flat lamellar ICM folds, closest to the cell periphery, while the LH2-only regions arise from the subsequently formed distal layers, as suggested by the size and density of intramembrane particles revealed by freeze-fracture TEM of whole cells (*38*). This possibility is also consistent with the sequence in which the complexes are assembled in the growing ICM (*73*).

Surprisingly, areas of smooth protein-free lipid bilayer were found in AFM topographs of cells grown under both high and low levels of illumination (*37*), while in membranes from high-light-adapted cells, paracrystalline domains of hexagonally packed core complexes were also observed (Figure 10D), reminiscent of the organization existing in the *Blc. viridis* ICM (Figure 1C). Although the origin of the apparently pure lipid bilayer is unknown, the core-only membrane domains may arise from the invaginating, stacked CM layer (Figure 10A), seen by freeze fracture to contain large, tightly packed particles (*38*), which may reflect preferential core assembly (*73*) in these regions.
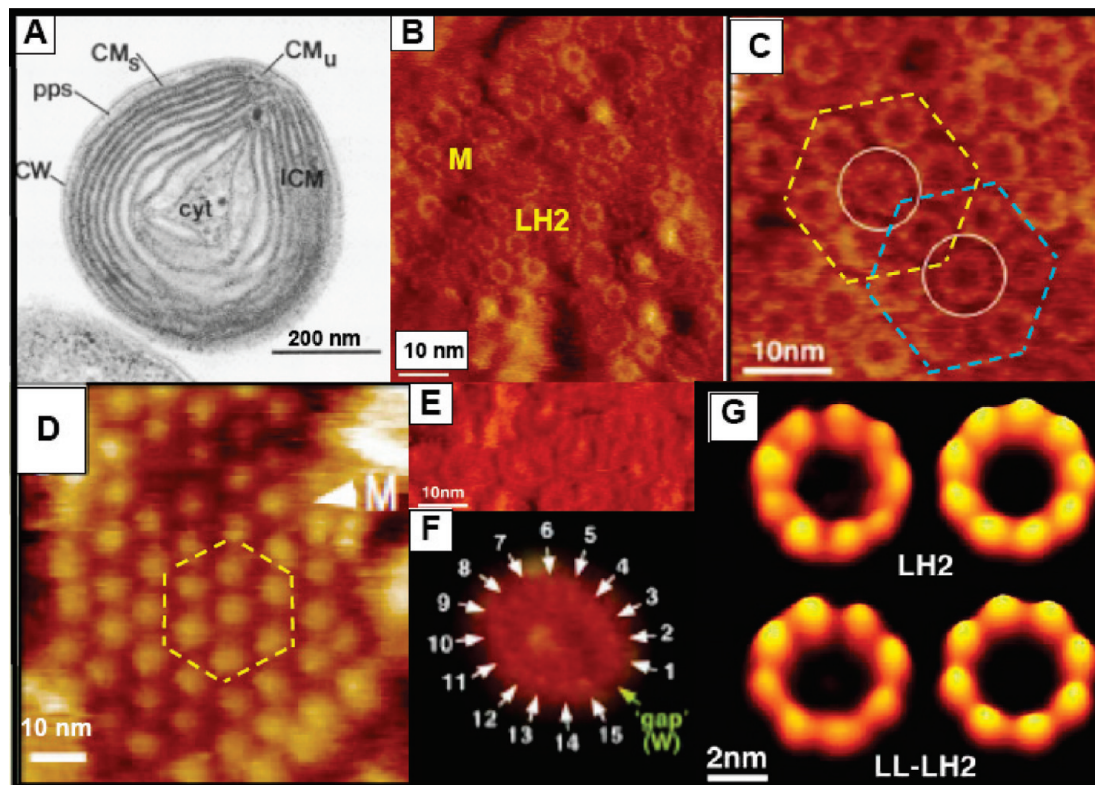
FIGURE 10: TEM and AFM analyses of *Rps. palustris* membranes. AFM topographs were obtained in contact mode essentially as described in the legend of Figure 1. (A) TEM cross section of a cell (*38*), showing the area filled with the stacked ICM arranged as appressed membrane layers around the cell periphery: clear areas within the stacks represent the lumenal spaces of each ICM sack, and the small area of the unstacked cytoplasmic membrane (CM_U) is seen at the intersection of two ends of the ICM stack. CM_S, stacked cytoplasmic membrane, representing a single CM layer appressed onto the outermost ICM layer; CW, cell wall; pps, periplasmic space. (B and C) AFM topographs of low-light cells (*37*). (B) Area of mixed LH2 and RC-LH1 core complexes arranged randomly in a ratio of ~1:3. M, monomeric RC-LH1 core complex. (C) Coexisting, hexagonally packed lattices of LH2 complexes. (D and E) AFM topographs of high-light cells. (D) Region of hexagonally packed, monomeric RC-LH1 core complexes. The protruding RC-H subunit is seen at the core complex surface. (E) Chain of connected, monomeric RC-LH1 core complexes. The H subunit has been removed by nanodissection, revealing underlying, randomly oriented L and M subunits. (F) High-resolution topograph of monomeric RC-LH1 core complexes, containing a gap in the LH1 15-mer of $\alpha\beta$-heterodimers, confirming the in situ existence of the elliptical LH1 arrangement modeled in the crystal structure of the *Rps. palustris* RC-LH1 complex (*25*). W, putative PufX homologue. (G) Nonsymmetrized (left) and symmetrized (right) averages of AFM images of LH2 (B800−850 type) nonameric rings, predominating at high light intensity, and LL-LH2, LH4 (high 800-type peripheral antenna) octameric rings (*74*), predominating at low light intensity. Panel A reproduced with permission from ref *38*. Copyright 1983 American Society for Microbiology. Panels B−G reproduced from ref *37*. Copyright 2006 Elsevier.

Other membrane domains in high-light membranes contained core complexes with randomly ordered RCs that were arranged in chains, along with a few LH2 complexes (Figure 10E); such a core arrangement would be expected to facilitate efficient energy trapping under conditions of high photon flux. The AFM images established an in situ structure for the core complex (Figure 10F), basically similar to the X-ray crystallography model (*25*), with an elliptical LH1 15-mer of $\alpha\beta$-heterodimers interrupted by a gap near the presumed location of W, a putative PufX homologue. The circular shape assumed by LH1 complexes after RC nanodissection demonstrates that the inner RC assembly induces the observed ellipticity upon the core complex (*37*).

Chromatic adaptation in *Rps. palustris* resulted in modifications both in near-IR antennae absorption and in the size of peripheral antenna rings when cells were switched from high to low light intensity (Figure 10G). Accordingly, LH4, a unique octameric, 800 nm light-absorbing peripheral antenna complex (*74*), regulated by a specific phytochrome (*75, 76*), is present under high-intensity illumination at approximately the same level as the nonameric LH2 complex,

while a 10-fold increase in the LH4 level relative to LH2 is found under low light.

(iv) Rba. blasticus. Although *Rba. blasticus* is closely related to *Rba. sphaeroides* and also contains the core-organizing PufX polypeptide, AFM topographs obtained with transversely oriented fused chromatophores showed that the photosynthetic complexes assume a more random organization (*34*) (not shown). The considerable mixing of LH2 and the mainly dimeric core components demonstrated that unlike that in *Rba. sphaeroides*, PufX does not play a long-range organizational role in this species. In high-resolution AFM images, an open S-shaped structure for the dimeric RC-LH1 core complex was clearly visualized, which was assumed to consist of 26 LH1 $\alpha\beta$-subunits, together with two PufX polypeptides in contact at the junction between the two halves of the structure; this interpretation is essentially similar to the PufX−PufX helix−helix model for the *Rba. sphaeroides* core particle (*52*).[2] Only higher-resolution structural data will determine whether the assignment of the position of PufX helices for *Rba. blasticus* (*34*) may actually reflect a genuine

species difference (see Figure 4 for details of the *Rba. sphaeroides* core dimer).

THE ELUSIVE ATP SYNTHASE AND CYTOCHROME *bc*₁ COMPLEXES

One of the more surprising aspects of AFM studies of bacterial photosynthetic membranes thus far has been the inability to visualize the F_1F_O-ATP synthase and cytochrome bc_1 complexes in any of the topographs obtained from a variety of purple bacteria,[3] despite ample biochemical and biophysical evidence that these protein complexes were present in imaged preparations (see below). A number of suggestions have been offered to explain this enigma (*3*), including the possibility that these complexes do not localize in the flat membrane regions adhering to the mica surface that are visualized by AFM but instead occupy more curved areas which form the poles of isolated ICM vesicles and are excluded from the imaged surfaces. In light of these considerations, a number of models based largely upon the observed AFM topographs have been formulated (see, e.g., Figure 3B), which places a single ATP synthase and a number of bc_1 complexes at the chromatophore poles outside regions crowded with the LH2 and RC-LH1 core complexes (*3, 77*), or within the CM at or near the neck of the in vivo ICM vesicles (*20, 21*), where rapid physiological adaptation between photosynthetically active and respiratory chain domains can occur (*78*).

ATP Synthase. The low number of ATP synthases per vesicle was largely based upon estimates in which an analysis of electrochromic carotenoid transients, both in the presence and in the absence of specific ATP synthase inhibitors, was interpreted to show that at most, only one ATP synthase was present per *Rhodobacter capsulatus* ICM vesicle (*79*). In contrast, a more recent approximation (*80*) suggested that on average, each chromatophore vesicle contains ~10 ATP synthases. The latter estimates were derived from both quantitative Western blotting and catalytic activity levels, and it was suggested that besides differences in chromatophore preparations, the low estimates made in ref *79* did not adequately reflect the levels of phosphorylating current present after the single flash used in generating the electrochromic response. However, in ref *80*, the flattening effects on vesicle diameter were not taken into account (resulting in an ~1.5-fold overestimate), and no distinction was made between the midplane and the surface of the vesicles. This means that the approximation of ~10 ATP synthases per chromatophore is likely to be an overestimate, perhaps by a factor of roughly 3. In the case of *Phs. molischianum*, however, it appears that the ATP synthase is largely localized in different membrane regions; communication between them

FIGURE 11: All four subunits of the cytochrome bc_1 complex are present in ICM patches of *Rba. sphaeroides*. Western blot of ICM patches: (left panel) antiserum raised against subunit IV (SuIV), cytochrome c_1 (cyt c_1), and the Rieske FeS protein (ISP) also appeared with increasing membrane concentrations; (right panel) antiserum containing cytochrome b (cyt b) and c_1 antibodies; both blots were performed at three different membrane concentrations. Electrophoretic separation and blotting procedures have been described previously (*46*).

via a single functionally continuous space connecting the stacked ICM and the periplasm, as demonstrated by the visualization of entrapped terbium chloride in TEM of thin-cell sections, may be sufficient for rapid proton diffusion (*81*).

In contrast to the negative results obtained with bacterial photosynthetic membranes, ATP synthase has recently been visualized at submolecular resolution in AFM topographs of the intermembrane surface of the native yeast mitochondrial inner membrane (*82*). These images showed that the F_O transmembrane sector forms dimeric structures that exist as rows of ATP synthase complexes, and it was suggested that such a supramolecular organization plays roles both in the stabilization of the F_O rotor–stator interface and in mitochondrial cristae morphogenesis. In contrast, the prokaryotic ATP synthase is thought to exist in a monomeric form (*83*).

Thus, in light of the revised estimates of ATP synthase content, and the ability to obtain surface views of the mitochondrial F_O machinery, it will be necessary to develop new strategies for visualizing the native enzyme in ICM preparations. One possibility is the use of spheroplast-derived vesicles obtained by osmotic lysis of *Rba. sphaeroides* (*84*), in which the periplasmic surface is exposed, equivalent to the intermembrane surface of the mitochondrial inner membrane. Spheroplast-derived vesicles are generally larger than chromatophores and have a tendency to form nested structures; this may ultimately permit direct AFM analysis as performed on the flattened surface of isolated membrane sacs supported by an underlying membrane (*1, 15, 37, 39*).

Cytochrome bc_1 Complex. Although the cytochrome bc_1 complex has yet to be detected by AFM, it has been estimated that a 70 nm *Rba. sphaeroides* chromatophore vesicle should contain 5–10 bc_1 dimers (*3*). Moreover, Figure 11 shows that all four subunits of the bc_1 complex were present in Western blots of the ICM patches that were analyzed by AFM, including subunit IV. This 14 kDa protein is believed to contain a single C-terminal transmembrane

---

[3] In the initial AFM topographs of the periplasmic surface of *Rsp. photometricum* photosynthetic membranes (*36*) in which the upper layer of these membrane vesicles was removed by nanodissection with the AFM tip, small protein-containing regions were observed that could not be readily assigned to LH2 or RC-LH1 core complexes. There was speculation that these regions might be the sites containing the cytochrome bc_1 complex, and a model based upon dimers of a three-subunit yeast complex was tentatively fitted to these images. Such topographical areas were not observed in subsequent images obtained directly on the cytoplasmic surface of native membranes (*39*), and it is possible that they arose from poorly resolved regions of LH complexes of heterogeneous size, or complexes in which protruding protein domains were removed during the nanodissection procedure.
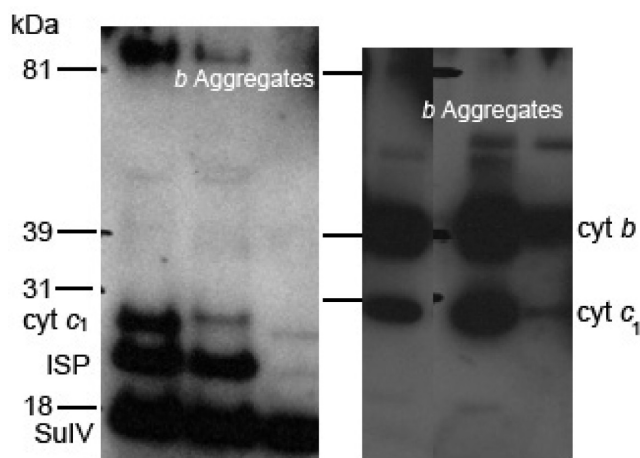
helix, with the globular bulk portion localized largely in the cytoplasm (*85, 86*). Unfortunately, subunit IV was apparently lost during crystallization of the *Rba. sphaeroides bc$_1$* complex and was thus absent from the recently reported crystal structure (*87*), which showed that the cytoplasmically localized segments of the three-subunit complex do not project out significantly from the bilayer surface. Thus, the availability of a high-resolution structural information for the large N-terminal portion of subunit IV would be expected to provide a possible signature for the AFM detection of the *bc$_1$* complex at the cytoplasmic surface of the ICM.

Since the cytochrome *bc$_1$* complex was also absent from AFM topographs obtained directly with native ICM samples from *Rsp. photometricum*, it is noteworthy that unattributed structures or gaps were absent over the large flat ICM areas that were imaged at submolecular resolution. These areas contained as many as 50 RCs (*69*), and given the expected stoichiometries, one would expect to have observed both the cytochrome *bc$_1$* and ATP synthase components. Both flash and steady-state spectroscopic measurements have established the presence of the *bc$_1$* complex in these membrane samples (*39*). Photooxidized cytochrome *c* was rapidly re-reduced after a saturating flash, and re-reduction was sensitive to the specific *bc$_1$* inhibitors myxothiazole and stigmatellin. In addition, steady-state reduction of myxothiazole-sensitive cytochrome *c* by ubiquinol 2 was also demonstrated in detergent-treated membranes (*70*). In the membrane preparations of *Phs. molischianum* imaged by AFM (*15*), which like *Rsp. photometricum* also forms a stacked, disclike ICM, a ratio of RC to cytochrome *bc$_1$* complex of 8:1 and a pool of ∼25 quinones was found, along with a slow quinol diffusion time from the RC to the *bc$_1$* complex of ∼260 ms (*81*). This can be compared to the rate of cytochrome *b$_{561}$* photoreduction of 10 ms in *Rba. sphaeroides* chromatophores (*88*) from the strain examined via AFM (*16*). These functional measurements suggest that lamellar ICM structures function very differently from the vesicular ICM of *Rba. sphaeroides*, being adapted to handle the slower diffusion rates of quinone redox species and the long-range movement of protons within the intra-ICM space.

The localization of the cytochrome *bc$_1$* complex at the neck of ICM vesicles (Figure 3B) or in adjacent CM regions, as suggested by its apparent absence from flat ICM regions imaged by AFM, would mean that for quinone redox species to participate in light-driven cyclic electron flow, bidirectional migration must occur within the hydrophobic lipid phase over large membrane bilayer distances between the RC and the *bc$_1$* complex. For *Rsp. photometricum*, it has been proposed on the basis of time-lapse AFM and Monte Carlo simulations that short-range corralled diffusion can occur in the disordered, more fluid ICM regions containing both LH2 and core complexes (*69*). Such a diffusion process is sufficient to allow the flow of quinols between the complexes, once they have exited from the RC Q$_B$ site and escaped through the LH1 annulus (see arrows in panels F and G of Figure 8). Subsequently, the long-range flow of metabolically active quinone species is augmented by their apparent exclusion from large ordered fields of static LH2 antenna in *Rsp. photometricum*. Because of the density of disordered domains of mixed complexes within the ICM (Figure 8A,C), relatively high turnover rates are maintained for cytochrome *bc$_1$* and core complexes that are sufficiently close.

A somewhat different picture of quinone migration has emerged from the AFM topographs of *Rba. sphaeroides*, in which a highly organized arrangement of photosynthetic complexes is observed (*16, 19*). A very limited lateral mobility of pigment−protein complexes was observed during repeated AFM scanning of ICM patches (*16*); however, in these single-membrane bilayer preparations, any integral membrane protein diffusion could be impeded by interactions with the mica surface. Nevertheless, it was suggested that lateral migration of individual components is probably restricted by the close packing of LH complexes. Subsequent AFM analysis of an LH2-only membrane demonstrated that sufficient space is available for phospholipid molecules between individual LH2 complexes (Figure 6C), thereby permitting the diffusion and shuttling of quinone redox species to foster efficient cyclic electron flow between the RC-LH1 core and physically remote cytochrome *bc$_1$* complexes, possibly via a channeling mechanism (*69*). In a recent ICM developmental study in *Rba. sphaeroides*, a correlation between the slowing of electron transport turnover rates and the formation of the LH2 antenna could be made (*73*). The extent to which this kinetic phenomenon arises from a crowding effect imposed by constraints on quinol/quinone flow as the growing ICM bilayer becomes packed with accumulating LH2 complexes or is related to an increased distance between the RC and *bc$_1$* complexes in the expanding ICM remains to be determined.

The likely positioning of the cytochrome *bc$_1$* complex some distance from most RCs in the mature ICM (*20, 21*), together with the tightly packed linear arrays of RC-LH1 core complexes observed by AFM (*16*), cannot be easily reconciled with an organization of the photosynthetic chain of *Rba. sphaeroides* into supercomplexes that consist of a dimeric *bc$_1$* complex sandwiched between two dimeric core complexes, interacting with a sequestered cytochrome *c$_2$* population (*89*; see, however, refs *3* and *90*). The supercomplex model was based largely on the thermodynamic equilibrium between the primary RC donor and the high-potential Rieske FeS protein and cytochrome *c$_1$* components of the *bc$_1$* complex thought to be mediated in <1 ms by the cytochrome *c$_2$* trapped in a single supercomplex. The impasse between these kinetic data and the supramolecular organization as imaged by AFM has recently been evaluated by Lavergne et al. (*91*), who suggested that mobile quinone carriers must undergo relatively long-range diffusion in species with a low *bc$_1$*:RC ratio, while supercomplexes would be expected to form in species with only high *bc$_1$*:RC ratios. It was also agreed that the flattening of membrane preparations necessary for obtaining suitable AFM topographs may be related to the inability to observe *bc$_1$* complexes, which would be excluded from these antenna-packed regions, and that supercomplexes may arise in more curved ICM regions or in the adjacent CM areas that are not amenable to the imaging process. While the possibility was raised that the *bc$_1$* complex could be expelled from the membrane bilayer during the process of flattening and adhering onto the mica support, it must be emphasized that this oxidoreductase is also not observed in AFM topographs obtained with membranes supported by an underlying bilayer, as discussed above (*1−4*). A possible role for protein interfaces in the channeling of quinone redox species is also discussed (*91*).
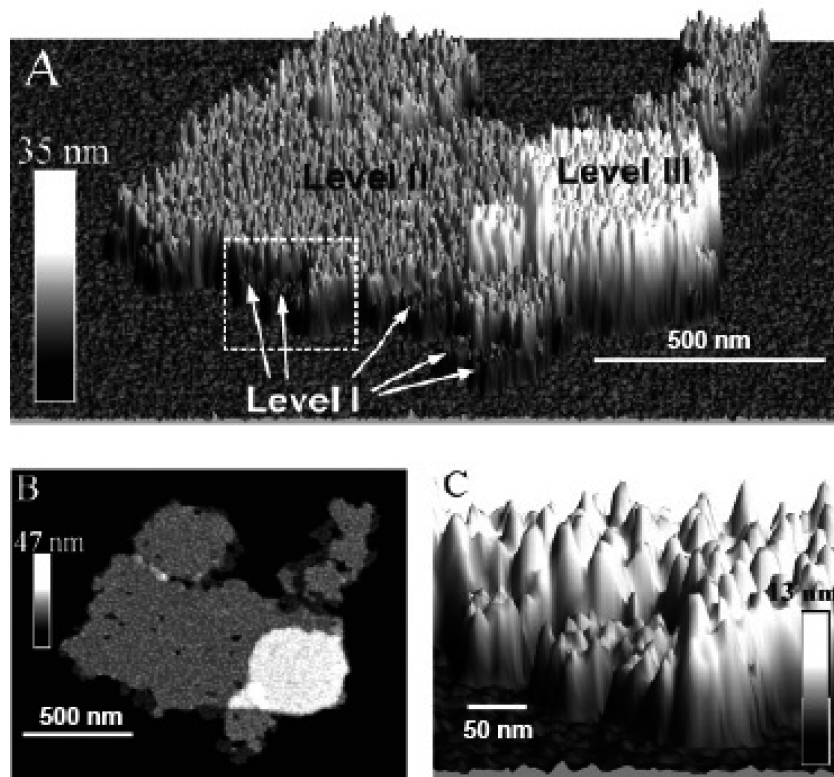
FIGURE 12: AFM topograph of stacked spinach grana membranes isolated from a thylakoid preparation (*96*). The images were obtained in air at a lateral resolution of ~4 nm with sample−tip interactions minimized by an active feedback control. (A) 3D representation of the AFM image, with discrete height levels indicated. (B) 2D representation of the same AFM image. (C) Enlarged region at height level I, demarcated by the white box in panel A. Reproduced with permission from ref *96*. Copyright 2008 American Chemical Society.

AFM STUDIES OF NATIVE CHLOROPLAST THYLAKOID MEMBRANES

The photosynthetic complexes of higher-plant chloroplasts are segregated into distinct regions within the chloroplast thylakoid membrane, where the stacked grana regions house oxygen-evolving photosystem (PS) II and light-harvesting complex (LHC) II; NADPH-generating PSI, the associated LHCI antenna, and the ATP synthase are found exclusively in the interconnecting, unstacked stroma lamellae, and the cytochrome b_6f complex is apparently distributed between both regions (*92*). Over the past several years, AFM has been applied to the analysis of envelope-free chloroplasts after chemical fixation, revealing details of the organization of PSI and the ATP synthase in stromal lamellae and at the grana margins, in which their surface density was highest (*93*). Subsequently, the degree of grana membrane stacking and the mean grana disc heights have been assessed by low-resolution AFM of isolated grana thylakoids (*94, 95*).

More recently, the detailed in situ organization of PSII was studied in stacked grana membrane regions by tapping mode AFM in air (*96*). As seen in 3D topographs (Figure 12A), protruding structures, identified as the PSII oxygen-evolving complex, are crowded together in a parallel alignment at three different levels over the lumenal membrane surface. Height measurements showed that levels I, II, and III represent a single grana membrane, two stacked membranes, and a four-membrane stack, respectively. The large area occupied by level II was thought to arise from the lateral fusion of several double-stacked grana discs over the mica surface, as suggested from the 2D representation of the AFM topograph (Figure 12B). The characteristic dense

packing of the protruding particles is seen in greater detail in the enlarged 3D representation of the level I structures shown in Figure 12C.

Comparison of the PSII distribution deduced from AFM with that derived from established TEM images of freeze-fracture replicas of thylakoid membranes showed that the AFM imaging of grana membranes in air does not significantly alter the organization and spacing of the complexes as assessed from the areas occupied by the oxygen-evolving complex (*96*). These spacings are apparently established by trimeric LHCII complexes. Analysis of the AFM data confirmed the nonrandom positioning of the PSII protrusions into an ordered pattern of a near-parallel organization that may reflect preferential interactions with LHCII at both the bottom and top surfaces of PSII−LHCII supercomplexes. The lumenal and stromal PSII protrusions in adjacent grana discs were displaced relative to one another, resulting in the creation of a protein-free area near the P680 reaction center Q_B binding site. Such a region within the thylakoid membrane is important for the efficient unbinding and binding of plastoquinonol and plastoquinone, as well as the accommodation of protein traffic essential for biogenesis of the photosynthetic apparatus, adaptation to stress, and the turnover and repair of damaged PSII components (*96*).

As a result of the organized protein arrangement in the crowded grana membrane, diffusion channels may be formed temporarily to facilitate the lateral mobility of a fraction of the PSII and LHCII complexes (*97*). Analysis of protein diffusion in grana thylakoids by fluorescence recovery after photobleaching indicated that while up to 75% of the Chl−protein complexes were essentially immobile, for the

remaining ∼25%, an exchange rate between grana and stroma lamellae of a few seconds was measured (*97*). This rapid and long-range movement of a portion of the protein population is dependent upon the considerable degree of structure within the native grana discs. This high level of molecular ordering arises from the organization of these Chl−protein complexes into PSII−LHCII supercomplexes, capable of ultimately forming semicrystalline structured assemblies over the entire grana disc. The limitation of the discs to diameters of less than or approximately 500 nm assures that diffusion times are sufficiently short to support the regulation of light-harvesting capabilities and repair of photodamaged PSII. Moreover, Monte Carlo simulations suggested that above a critical protein density (percolation threshold of 60−70%) in the crowded grana membrane, plastoquinone diffusion is confined to small lipid regions making up diffusion microdomains, surrounded by LHCII, PSII, and the b_6f complex (*97*). An analysis of plastoquinone motion in the lipid-phase diffusion space by percolation theory showed that the average travel time from a given PSII to the next b_6f complex was ∼8 ms, nearly 3 orders of magnitude slower than in an obstacle-free membrane (*98*). The molecular crowding accounting for this significant retardation of diffusion processes may be overcome by formation of supercomplexes and lipid-spaced supermolecular ordering, which remove the barriers to plastoquinone diffusion (*99*). These factors, together with limitations on grana disc size, were the likely evolutionary pressures that ensured the development of rapid and efficient mechanisms for lateral membrane transport.

CONCLUDING REMARKS AND FUTURE PROSPECTS

Although X-ray crystallography has greatly improved our knowledge of both the molecular structure and functional mechanisms of individual BChl−protein complexes (*11−13, 23−25, 51*), AFM studies now permit the direct visualization of their in situ supramolecular organization and associations over the ICM surface (*1−4*), thereby providing an expanding global structural picture within their native membrane environments. Significant insights into the detailed structural and functional properties of these integrated systems has also arisen from the successful docking of molecular structures into the AFM images of the LH2 and RC-LH1 core complexes (*4, 14*), as well as their application in atomic-resolution modeling efforts (*20, 21, 66*). As such, AFM has matured into a powerful technique, proving to be entirely complementary to X-ray crystallography and TEM as a highly informative membrane protein research tool capable of providing useful and novel structural information.

In the study of photosynthetic membranes, it is clear that AFM has raised a number of questions that still require answers. First and foremost is the perplexing problem of the location of the cytochrome bc_1 complex and the ATP synthase posed by the initial studies reported here. Second and perhaps more interestingly is why are they so difficult to observe. Help in answering questions about how photosynthetic systems are assembled should also be provided by AFM. These different lines of investigation are currently being actively pursued in our laboratories.

Several obstacles remain before the full power of AFM imaging can be brought to bear on the study of other membrane types. In particular, photosynthetic membranes offer the advantage of being very rich in proteins with a packing density of up to 77% (*37*), and the structures of these different proteins are known. This pair of factors assures that the proteins move very little during the acquisition of images (*69*) and that they can be readily identified by their form. Nevertheless, several other types of native membranes have recently been imaged at high resolution by using AFM (*82, 100, 101*), which has yielded pertinent information about the large-scale protein organization in the mitochondrial inner (*82*) and outer membrane (*101*) and lens membranes (*100*). Unfortunately, the conditions of both identifiable and static proteins are not frequently met, and many membrane types are not well adapted to AFM imaging. However, currently progress is being made in two different directions that should allow AFM to be used for the imaging of other types of native membranes: (1) molecular recognition using the AFM tip to identify the imaged molecule (*102*) and (2) high-speed AFM to permit the visualization of the more dynamic systems (*103*).

Through the development of recognition imaging techniques, e.g., by exploiting highly specific antibody−antigen (*102*) and receptor−ligand interactions (*104*), the problem of identifying molecules by AFM can be attacked through functionalizing the tip. The relevance of such techniques to studies of dynamic processes in biological membranes will be enhanced when they can be used in combination with more rapid AFM scanning. Performing AFM at higher speeds increases the time resolution from near 60 s per image by 3 orders of magnitude to ∼60 ms per image (*103*). This increased time resolution allows the imaging of more dynamic systems that cannot be visualized by a slower raster imaging system, where coherence between the different scan lines is required. Importantly, this increase in time resolution for a small scan area (typically 250 nm × 250 nm) means that membrane proteins with diffusion coefficients as high as ∼10^{-10} cm^2 s^{-1} can be reasonably imaged. Together, we anticipate that these approaches will permit the high-resolution imaging of native membranes from more diverse sources and the identification of their different components.

In conclusion, AFM offers a method with increasingly wide applicability for studies of the large-scale organization and dynamics of biological membranes and will continue to advance our understanding of numerous fundamental biological processes. In this connection, a recent review on the use of AFM as an important nanotool in membrane biology (*105*) describes a number of developing strategies for visualizing the molecular machineries of cellular membranes and determining how they are directed and controlled. Among the most promising that are likely to find application in the further elucidation of the structure and function of photosynthetic membranes are new methods that allow the observation and manipulation of cellular membrane machineries at the AFM tip, such as measurements of local membrane elasticity, adhesive forces, conformational flexibility and functional states of membrane proteins, and molecular interactions that drive membrane assembly and the dynamic adaptation of membranes to different environmental states. Moreover, the relationship between structural information at submolecular resolution obtained by AFM and functional correlates when used in conjunction with confocal fluorescence microscopy provides the basis for simultaneous

optical and topographical imaging at the single-molecule level (*106*). Accordingly, we can envision that with the combined use of these techniques, it will be possible to integrate the molecular topography of individual developing complexes with their specific fluorescence emission spectra. Altogether, such novel and innovative strategies (*105*) will continue to make contributions to the emerging revolution in membrane biology that has already been sparked by AFM.

REFERENCES

1. Scheuring, S., Levy, D., and Rigaud, J. L. (2005) Watching the components of photosynthetic bacterial membranes and their in situ organisation by atomic force microscopy. *Biochim. Biophys. Acta 1712*, 109–127.
2. Sturgis, J. N., and Niederman, R. A. (2008) Atomic force microscopy reveals multiple patterns of antenna organization in purple bacteria: Implications for energy transduction mechanisms and membrane modeling. *Photosynth. Res. 95*, 269–278.
3. Sturgis, J. N., and Niederman, R. A. (2008) Organization and Assembly of Light-Harvesting Complexes in the Purple Bacterial Membrane. In *The Purple Phototrophic Bacteria. Advances in Photosynthesis and Respiration* (Hunter, C. N., Daldal, F., Thurnauer, M. C., and Beatty, J. T., Eds.) Vol. 28, pp 253−273, Springer, Dordrecht, The Netherlands.
4. Scheuring, S. (2008) The Supramolecular Assembly of the Photosynthetic Apparatus of Purple Bacteria Investigated by High-Resolution Atomic Force Microscopy. In *The Purple Phototrophic Bacteria. Advances in Photosynthesis and Respiration* (Hunter, C. N., Daldal, F., Thurnauer, M. C., and Beatty, J. T., Eds.) Vol. 28, pp 941−952, Springer, Dordrecht, The Netherlands.
5. Miller, K. R. (1979) Structure of a bacterial photosynthetic membrane. *Proc. Natl. Acad. Sci. U.S.A. 76*, 6415–6419.
6. Stark, W., Kühlbrandt, W., Wildhaber, I., Wehrli, E., and Mühlethaler, K. (1984) The structure of the photoreceptor unit of *Rhodopseudomonas viridis*. *EMBO J. 3*, 777–783.
7. Welte, W., and Kreutz, W. (1982) Formation, structure and composition of a planar hexagonal lattice composed of specific proteinlipid complexes in the thylakoid membranes of *Rhodopseudomonas viridis*. *Biochim. Biophys. Acta 692*, 479–488.
8. Vos, M., van Dorssen, R. J., Amesz, J., van Grondelle, R., and Hunter, C. N. (1988) The organisation of the photosynthetic apparatus of *Rhodobacter sphaeroides*: Studies of antenna mutants using singlet-singlet quenching. *Biochim. Biophys. Acta 933*, 132–140.
9. Vos, M., van Grondelle, R., van der Kooij, F. W., van de Poll, D., Amesz, J., and Duysens, L. M. N. (1986) Singlet-singlet annihilation at low temperatures in the antenna of purple bacteria. *Biochim. Biophys. Acta 850*, 501–512.
10. Westerhuis, W. H. J., Vos, M., van Grondelle, R., Amesz, J., and Niederman, R. A. (1998) Altered organization of light-harvesting complexes in phospholipid-enriched *Rhodobacter sphaeroides* chromatophores as determined by fluorescence yield and singlet-singlet annihilation measurements. *Biochim. Biophys. Acta 1366*, 317–329.
11. Katona, G., Andreasson, U., Landau, E. M., Andreasson, L. E., and Neutze, R. (2003) Lipidic cubic phase crystal structure of the photosynthetic reaction centre from *Rhodobacter sphaeroides* at 2.35 Å resolution. *J. Mol. Biol. 331*, 681–692.
12. McDermott, G., Prince, S. M., Freer, A. A., Hawthornthwaite-Lawless, A. M., Papiz, M. Z., Cogdell, R. J., and Isaacs, N. W. (1995) Crystal structure of an integral membrane light-harvesting complex from photosynthetic bacteria. *Nature 374*, 517–521.
13. Koepke, J., Hu, X. C., Muenke, C., Schulten, K., and Michel, H. (1996) The crystal structure of the light-harvesting complex II (B800−850) from *Rhodospirillum molischianum*. *Structure 4*, 581–597.
14. Scheuring, S., Boudier, T., and Sturgis, J. N. (2007) From high-resolution AFM topographs to atomic models of supramolecular assemblies. *J. Struct. Biol. 159*, 268–276.
15. Gonçalves, R. P., Bernadac, A., Sturgis, J. N., and Scheuring, S. (2005) Architecture of the native photosynthetic apparatus of *Phaeospirillum molischianum*. *J. Struct. Biol. 152*, 221–228.
16. Bahatyrova, S., Frese, R. N., Siebert, C. A., Olsen, J. D., van der Werf, K. O., van Grondelle, R., Niederman, R. A., Bullough, P. A., Otto, C., and Hunter, C. N. (2004) The native architecture of a photosynthetic membrane. *Nature 430*, 1058–1062.
17. Frese, R. N., Olsen, J. D., Branvall, R., Westerhuis, W. H. J., Hunter, C. N., and van Grondelle, R. (2000) The long-range supraorganization of the bacterial photosynthetic unit: A key role for PufX. *Proc. Natl. Acad. Sci. U.S.A. 97*, 5197–5202.
18. Frese, R. N., Siebert, C. A., Niederman, R. A., Hunter, C. N., Otto, C., and van Grondelle, R. (2004) The long-range organization of a native photosynthetic membrane. *Proc. Natl. Acad. Sci. U.S.A. 101*, 17994–17999.
19. Frese, R. N., Pàmies, J. C., Olsen, J. D., Bahatyrova, S., van der Weij-de Wit, C. D., Aartsma, T. J., Otto, C., Hunter, C. N., Frenkel, D., and van Grondelle, R. (2008) Protein shape and crowding drive domain formation and curvature in biological membranes. *Biophys. J. 94*, 640–647.
20. Sener, M. K., Olsen, J. D., Hunter, C. N., and Schulten, K. (2007) Atomic-level structural and functional model of a bacterial photosynthetic membrane vesicle. *Proc. Natl. Acad. Sci. U.S.A. 104*, 15723–15728.
21. Sener, M. K., and Schulten, K. (2008) From Atomic-Level Structure to Supramolecular Organization in the Photosynthetic Unit of Purple Bacteria. In *The Purple Phototrophic Bactria. Advances in Photosynthesis and Respiration* (Hunter, C. N., Daldal, F., Thurnauer, M. C., and Beatty, J. T., Eds.) Vol. 28, pp 275−294, Springer, Dordrecht, The Netherlands.
22. Olsen, J. D., Tucker, J. D., Timney, J. A., Qian, P., Vassilev, C., and Hunter, C. N. (2008) The organization of LH2 complexes in membranes from *Rhodobacter spaheroides*. *J. Biol. Chem. 283*, 30772–30779.
23. Deisenhofer, J., and Michel, H. (1989) The photosynthetic reaction center from the purple bacterium *Rhodopseudomonas vridis*. *Science 245*, 1463–1473.
24. Allen, J. P., Feher, G., Yeates, T. O., Komiya, H., and Rees, D. C. (1987) Structure of the reaction center from *Rhodobacter sphaeroides* R26: The protein subunits. *Proc. Natl. Acad. Sci. U.S.A. 84*, 6162–6166.
25. Roszak, A. W., Howard, T. D., Southall, J., Gardiner, A. T., Law, C. J., Isaacs, N. W., and Cogdell, R. J. (2003) Crystal structure of the RC-LH1 core complex from *Rhodopseudomonas palustris*. *Science 302*, 1969–1972.
26. Scheuring, S., Reiss-Husson, F., Engel, A., Rigaud, J. L., and Ranck, J. L. (2001) High-resolution AFM topographs of *Rubrivivax gelatinosus* light-harvesting complex LH2. *EMBO J. 20*, 3029–3035.
27. Scheuring, S., Seguin, J., Marco, S., Levy, D., Breyton, C., Robert, B., and Rigaud, J. L. (2003) AFM characterization of tilt and intrinsic flexibility of *Rhodobacter sphaeroides* light harvesting complex 2 (LH2). *J. Mol. Biol. 325*, 569–580.
28. Bahatyrova, S., Frese, R. N., van der Werf, K. O., Otto, C., Hunter, C. N., and Olsen, J. D. (2004) Flexibility and size heterogeneity of the LH1 light harvesting complex revealed by atomic force microscopy: Functional significance for bacterial photosynthesis. *J. Biol. Chem. 279*, 21327–21333.
29. Gonçalves, R. P., Busselez, J., Lévy, D., Seguin, J., and Scheuring, S. (2005) Membrane insertion of *Rhodopseudomonas acidophila* light harvesting complex 2 investigated by high resolution AFM. *J. Struct. Biol. 149*, 79–86.
30. Stamouli, A., Kafi, S., Klein, D. C. G., Oosterkamp, T. H., Frenken, J. W. M., Cogdell, R. J., and Aartsma, T. J. (2003) The ring structure and organization of light harvesting 2 complexes in a reconstituted lipid bilayer, resolved by atomic force microscopy. *Biophys. J. 84*, 2483–2491.
31. Liu, L. N., Aartsma, T. J., and Frese, R. N. (2008) Dimers of light-harvesting complex 2 from *Rhodobacter sphaeroides* characterized in reconstituted 2D crystals with atomic force microscopy. *FEBS J. 275*, 3157–3166.
32. Siebert, C. A., Qian, P., Fotiadis, D., Engel, A., Hunter, C. N., and Bullough, P. A. (2004) Molecular architecture of photosynthetic membranes in *Rhodobacter sphaeroides*: The role of PufX. *EMBO J. 23*, 690–700.
33. Fotiadis, D., Qian, P., Philippsen, A., Bullough, P. A., Engel, A., and Hunter, C. N. (2004) Structural analysis of the reaction center light-harvesting complex I photosynthetic core complex of *Rhodospirillum rubrum* using atomic force microscopy. *J. Biol. Chem. 279*, 2063–2068.
34. Scheuring, S., Busselez, J., and Lévy, D. (2005) Structure of the dimeric PufX-containing core complex of *Rhodobacter blasticus* by in situ atomic force microscopy. *J. Biol. Chem. 280*, 1426–1431.

35. Scheuring, S., Seguin, J., Marco, S., Levy, D., Robert, B., and Rigaud, J.-L. (2003) Nanodissection and high-resolution imaging of the *Rhodopseudomonas viridis* photosynthetic core complex in native membranes by AFM. *Proc. Natl. Acad. Sci. U.S.A. 100*, 1690–1693.

36. Scheuring, S., Sturgis, J. N., Prima, V., Bernadac, A., Lévy, D., and Rigaud, J.-L. (2004) Watching the photosynthetic apparatus in native membranes. *Proc. Natl. Acad. Sci. U.S.A. 101*, 11293–11297.

37. Scheuring, S., Goncalves, R. P., Prima, V., and Sturgis, J. N. (2006) The photosynthetic apparatus of *Rhodopseudomonas palustris*: Structures and organization. *J. Mol. Biol. 358*, 83–96.

38. Varga, A. R., and Staehelin, L. A. (1983) Spatial differentiation in photosynthetic and non-photosynthetic membranes of *Rhodopseudomonas palustris*. *J. Bacteriol. 154*, 1414–1430.

39. Scheuring, S., and Sturgis, J. N. (2005) Chromatic adaptation of photosynthetic membranes. *Science 309*, 484–487.

40. Ostafin, A. E., Ponomarenko, N. S., Popova, J. A., Jäger, M., Bylina, E. J., and Norris, J. R. (2003) Characterization of expressed pigmented core light-harvesting complex (LH 1) in a reaction center deficient mutant of *Blastochloris viridis*. *Photosynth. Res. 77*, 53–68.

41. Ikeda-Yamasaki, I., Odahara, T., Mitsuoka, K., Fujiyoshi, Y., and Murata, K. (1998) Projection map of the reaction center-light harvesting 1 complex from *Rhodopseudomonas viridis* at 10 Å resolution. *FEBS Lett. 425*, 505–508.

42. Hunter, C. N., Tucker, J. D., and Niederman, R. A. (2005) The assembly and organisation of photosynthetic membranes in *Rhodobacter sphaeroides*. *Photochem. Photobiol. Sci. 4*, 1023–1027.

43. Cogdell, R. J., Gardiner, A. T., Roszak, A. W., Law, C. J., Southall, J., and Isaacs, N. W. (2004) Rings, ellipses and horseshoes: How purple bacteria harvest solar energy. *Photosynth. Res. 81*, 207–214.

44. Hunter, C. N., Pennoyer, J. D., Sturgis, J. N., Farrelly, D., and Niederman, R. A. (1988) Oligomerization states and associations of light-harvesting pigment-protein complexes of *Rhodobacter sphaeroides* as analyzed by lithium dodecyl sulfate-polyacrylamide gel electrophoresis. *Biochemistry 27*, 3459–3467.

45. Kiley, P. J., Varga, A., and Kaplan, S. (1988) Physiological and structural analysis of light-harvesting mutants of *Rhodobacter sphaeroides*. *J. Bacteriol. 170*, 1103–1115.

46. Westerhuis, W. H. J., Sturgis, J. N., Ratcliffe, E. C., Hunter, C. N., and Niederman, R. A. (2002) Isolation, size estimates, and spectral heterogeneity of an oligomeric series of light-harvesting 1 complexes from *Rhodobacter sphaeroides*. *Biochemistry 41*, 8698–8707.

47. Jungas, C., Ranck, J.-L., Rigaud, J.-L., Joliot, P., and Vermeglio, A. (1999) Supramolecular organization of the photosynthetic apparatus of *Rhodobacter sphaeroides*. *EMBO J. 18*, 534–542.

48. Bullough, P. A., Qian, P., and Hunter, C. N. (2008) Reaction Center-Light Harvesting Core Complexes of Purple Bacteria. In *The Purple Phototrophic Bactria. Advances in Photosynthesis and Respiration* (Hunter, C. N., Daldal, F., Thurnauer, M. C., and Beatty, J. T., Eds.) Vol. 28, pp 155–179, Springer, Dordrecht, The Netherlands.

49. Qian, P., Hunter, C. N., and Bullough, P. A. (2005) The 8.5 Å projection structure of the core RC-LH1-PufX dimer of *Rhodobacter sphaeroides*. *J. Mol. Biol. 349*, 948–960.

50. Qian, P., Bullough, P. A., and Hunter, C. N. (2008) Three-dimensional reconstruction of a membrane-bending complex: The RC-LH1-PufX core dimer of *Rhodobacter sphaeroides*. *J. Biol. Chem. 283*, 14002–14011.

51. Papiz, M. Z., Prince, S. M., Howard, T., Cogdell, R. J., and Isaacs, N. W. (2003) The structure and thermal motion of the B800–850 LH2 complex from *Rhodopsedomonas acidophila* at 2.0 Å resolution and 100 K: New structural features and functionally relevant motions. *J. Mol. Biol. 326*, 1523–1538.

52. Scheuring, S., Francia, F., Busselez, J., Melandri, B. A., Rigaud, J.-L., and Lévy, D. (2004) Structural role of PufX in the dimerization of the photosynthetic core complex of *Rhodobacter sphaeroides*. *J. Biol. Chem. 279*, 3620–3626.

53. Recchia, P. A., Davis, C. M., Lilburn, T. G., Beatty, J. T., Parkes-Loach, P. S., Hunter, C. N., and Loach, P. A. (1998) Isolation of the PufX protein from *Rhodobacter capsulatus* and *Rhodobacter sphaeroides*: Evidence for its interaction with the α-polypeptide of the core light-harvesting complex. *Biochemistry 37*, 11055–11063.

54. Barz, W. P., Vermeglio, A., Francia, F., Venturoli, G., Melandri, B. A., and Oesterhelt, D. (1995) Role of the PufX protein in photosynthetic growth of *Rhodobacter sphaeroides*. 2. PufX is required for efficient ubiquinone/ubiquinol exchange between the reaction center Q_B site and the cytochrome bc1 complex. *Biochemistry 34*, 15248–15258.

55. Tunnicliffe, R. B., Ratcliffe, E. C., Hunter, C. N., and Williamson, M. P. (2006) The solution structure of the PufX polypeptide from *Rhodobacter sphaeroides*. *FEBS Lett. 580*, 6967–6971.

56. Francia, F., Dezi, M., Rebecchi, A., Mallardi, A., Palazzo, G., Melandri, B. A., and Venturoli, G. (2004) Light-harvesting complex 1 stabilizes $P^+Q_B^-$ charge separation in reaction centers of *Rhodobacter sphaeroides*. *Biochemistry 43*, 14199–14210.

57. Dezi, M., Francia, F., Mallardi, A., Colafemmina, G., Palazzo, G., and Venturoli, G. (2007) Stabilization of charge separation and cardiolipin confinement in antenna-reaction center complexes purified from *Rhodobacter sphaeroides*. *Biochim. Biophys. Acta 1767*, 1041–1056.

58. Francia, F., Wang, J., Venturoli, G., Melandri, B. A., Barz, W. P., and Oesterhelt, D. (1999) The reaction center-LH1 antenna complex of *Rhodobacter sphaeroides* contains one PufX molecule which is involved in dimerization of this complex. *Biochemistry 38*, 6834–6845.

59. Francia, F., Wang, J., Zischka, H., Venturoli, G., and Oesterhelt, D. (2002) Role of the N- and C-terminal regions of the PufX protein in the structural organization of the photosynthetic core complex of *Rhodobacter sphaeroides*. *Eur. J. Biochem. 269*, 1877–1885.

60. Farchaus, J. W., and Oesterhelt, D. (1989) A *Rhodobacter sphaeroides* puf L, M and X deletion mutant and its complementation in trans with a 5.3 kb puf operon shuttle fragment. *EMBO J. 8*, 47–54.

61. Lilburn, T. G., Haith, C. E., Prince, R. C., and Beatty, J. T. (1992) Pleiotropic effects of *pufX* gene deletion on the structure and function of the photosynthetic apparatus of *Rhodobacter capsulatus*. *Biochim. Biophys. Acta 1100*, 160–170.

62. Holden-Dye, K., Crouch, L. I., and Jones, M. R. (2008) Structure, function and interactions of the PufX protein. *Biochim. Biophys. Acta 1777*, 613–630.

63. Allen, J. P., Feher, G., Yeates, T. O., Komiya, H., and Rees, D. C. (1987) Structure of the reaction center from *Rhodobacter sphaeroides* R-26: The cofactors. *Proc. Natl. Acad. Sci. U.S.A. 84*, 5730–5734.

64. Eldridge, M. D., Madden, P. A., and Frenkel, D. (1993) Entropy-driven formation of a superlattice in hard-sphere binary mixture. *Nature 365*, 35–37.

65. Sturgis, J. N., and Niederman, R. A. (1996) The effect of different levels of the B800–850 light-harvesting complex on intracytoplasmic membrane development in *Rhodobacter sphaeroides*. *Arch. Microbiol. 165*, 235–242.

66. Chandler, D. E., Hsin, J., Harrison, C. B., Gumbart, J., and Schulten, K. (2008) Intrinsic curvature properties of photosynthetic proteins in chromatophores. *Biophys. J. 95*, 2822–2836.

67. Kwa, L. G., Wegmann, D., Brügger, B., Wieland, F. T., Wanner, G., and Braun, P. (2008) Mutation of a single residue, β-glutamate-20, alters protein-lipid interactions of light harvesting complex II. *Mol. Microbiol. 67*, 63–77.

68. Agarwal, R., Rizvi, A. H., Prall, B. S., Olsen, J. D., Hunter, C. N., and Fleming, G. R. (2002) Nature of disorder and inter-complex energy transfer in LH2 at room temperature: A three pulse photon echo peak shift study. *J. Phys. Chem. A 106*, 7573–7578.

69. Scheuring, S., and Sturgis, J. N. (2006) Dynamics and diffusion in photosynthetic membranes from *Rhodospirillum photometricum*. *Biophys. J. 91*, 3707–3717.

70. Scheuring, S., Rigaud, J. L., and Sturgis, J. N. (2004) Variable LH2 stoichiometry and core clustering in native membranes of *Rhodospirillum photometricum*. *EMBO J. 23*, 4127–4133.

71. Westerhuis, W. H. J., Xiao, Z., and Niederman, R. A. (1992) Oligomerization-State Dependent Spectroscopic Properties of the B850 Light-Harvesting Complex of Rhodobacter sphaeroides R-26.1. In *Research in Photosynthesis* (Murata, N., Ed.) pp 93–96, Kluwer Academic Publishers, Boston.

72. Hu, X. C., Ritz, T., Damjanovic, A., Autenrieth, F., and Schulten, K. (2002) Photosynthetic apparatus of purple bacteria. *Q. Rev. Biophys. 35*, 1–62.

73. Koblízek, M., Shih, J. D., Breitbart, S. I., Ratcliffe, E. C., Kolber, Z. S., Hunter, C. N., and Niederman, R. A. (2005) Sequential assembly of photosynthetic units in *Rhodobacter sphaeroides* as

revealed by fast repetition rate analysis of variable bacteriochlorophyll a fluorescence. *Biochim. Biophys. Acta 1706*, 220–231.

74. Hartigan, N., Tharia, H. A., Sweeney, F., Lawless, A. M., and Papiz, M. Z. (2002) The 7.5-Å electron density and spectroscopic properties of a novel low-light B800 LH2 from *Rhodopseudomonas palustris*. *Biophys. J. 82*, 963–977.

75. Evans, K., Fordham-Skelton, A. P., Mistry, H., Reynolds, C. D., Lawless, A. M., and Papiz, M. Z. (2005) A bacteriophytochrome regulates the synthesis of LH4 complexes in *Rhodopseudomonas palustris*. *Photosynth. Res. 85*, 169–180.

76. Giraud, E., Zappa, S., Vuillet, L., Adriano, J. M., Hannibal, L., Fardoux, J., Berthomieu, C., Bouyer, P., Pignol, D., and Verméglio, A. (2005) A new type of bacteriophytochrome acts in tandem with a classical bacteriophytochrome to control the antennae synthesis in *Rhodopseudomonas palustris*. *J. Biol. Chem. 280*, 32389–32397.

77. Geyer, T., and Helms, V. (2006) A spatial model of the chromatophore vesicles of *Rhodobacter sphaeroides* and the position of the cytochrome bc_1 complex. *Biophys. J. 91*, 921–926.

78. Drews, G., and Niederman, R. A. (2002) Membrane biogenesis in anoxygenic photosynthetic prokaryotes. *Photosynth. Res. 73*, 87–94.

79. Feniouk, B. A., Cherepanov, D. A., Voskoboynikova, N. E., Mulkidjanian, A. Y., and Junge, W. (2002) Chromatophore vesicles of *Rhodobacter capsulatus* contain on average one F_OF_1-ATP synthase each. *Biophys. J. 82*, 1115–1122.

80. Gubellini, F., Francia, F., Turina, P., Lévy, D., Venturoli, G., and Melandri, B. A. (2007) Heterogeneity of photosynthetic membranes from *Rhodobacter capsulatus*: Size dispersion and ATP synthase distribution. *Biochim. Biophys. Acta 1767*, 1340–1352.

81. Mascle-Allemand, C., Lavergne, J., Bernadac, A., and Sturgis, J. N. (2008) Organisation and function of the *Phaeospirillum molischianum* photosynthetic apparatus. *Biochim. Biophys. Acta 1777*, 1552–1559.

82. Buzhynskyy, N., Sens, P., Prima, V., Sturgis, J. N., and Scheuring, S. (2007) Rows of ATP synthase dimers in native mitochondrial inner membranes. *Biophys. J. 93*, 2870–2876.

83. Strauss, M., Hofhaus, G., Schröder, R. R., and Kühlbrandt, W. (2008) Dimer ribbons of ATP synthase shape the inner mitochondrial membrane. *EMBO J. 27*, 1154–1160.

84. Takemoto, J., and Bachmann, R. C. (1979) Orientation of chromatophores and spheroplast-derived membrane vesicles of *Rhodopseudomonas sphaeroides*: Analysis by localization of enzyme activities. *Arch. Biochem. Biophys. 195*, 526–534.

85. Wu, J., and Niederman, R. A. (1995) Topological organization of the Rieske iron-sulphur protein and subunit IV in the cytochrome bc_1 complex of *Rhodobacter sphaeroides*. *Biochem. J. 305*, 823–828.

86. Tso, S. C., Shenoy, S. K., Quinn, B. N., and Yu, L. (2000) Subunit IV of cytochrome bc_1 complex from *Rhodobacter sphaeroides*: Localization of regions essential for interaction with the three-subunit core complex. *J. Biol. Chem. 275*, 15287–15294.

87. Esser, L., Elberry, M., Zhou, F., Yu, C. A., Yu, L., and Xia, D. (2008) Inhibitor-complexed structures of the cytochrome bc_1 from the photosynthetic bacterium *Rhodobacter sphaeroides*. *J. Biol. Chem. 283*, 2846–2857.

88. Bowyer, J. R., Hunter, C. N., Ohnishi, T., and Niederman, R. A. (1985) Photosynthetic membrane development in *Rhodopseudomonas sphaeroides*: Spectral and kinetic characterization of redox components of light-driven electron flow in apparent photosynthetic membrane growth initiation sites. *J. Biol. Chem. 260*, 3295–3304.

89. Joliot, P., Joliot, A., and Verméglio, A. (2005) Fast oxidation of the primary electron acceptor under anaerobic conditions requires the organization of the photosynthetic chain of *Rhodobacter sphaeroides* in supercomplexes. *Biochim. Biophys. Acta 1706*, 204–214.

90. Crofts, A., Guergova-Kuras, M., and Hong, S. J. (1998) Chromatophore heterogeneity explains phenomena seen in *Rhodobacter sphaeroides* previously attributed to supercomplexes. *Photosynth. Res. 55*, 357–362.

91. Lavergne, J., Verméglio, A., and Joliot, P. (2008) Functional Coupling Between Reaction Centers and Cytochrome bc1 Complexes. In *The Purple Phototrophic Bacteria. Advances in Photosynthesis and Respiration* (Hunter, C. N., Daldal, F., Thurnauer, M. C., and Beatty, J. T., Eds.) Vol. 28, pp 509–536, Springer, Dordrecht, The Netherlands.

92. Shimoni, E., Rav-Hon, O., Ohad, I., Brumfeld, V., and Reich, Z. (2005) Three-dimensional organization of higher-plant chloroplast thylakoid membranes revealed by electron tomography. *Plant Cell 17*, 2580–2586.

93. Kaftan, D., Brumfeld, V., Nevo, R., Scherz, A., and Reich, Z. (2002) From chloroplasts to photosystems: *In situ* scanning force microscopy on intact thylakoid membranes. *EMBO J. 21*, 6146–6153.

94. Gradinaru, C. C., Martinsson, P., Aartsma, T. J., and Schmidt, T. (2004) Simultaneous atomic-force and two-photon fluorescence imaging of biological specimens in vivo. *Ultramicroscopy 99*, 235–245.

95. Kirchhoff, H., Borinski, M., Lenhert, S., Chi, L. F., and Büchel, C. (2004) Transversal and lateral exciton energy transfer in grana thylakoids of spinach. *Biochemistry 43*, 14508–14516.

96. Kirchhoff, H., Lenhert, S., Büchel, C., Chi, L., and Nield, J. (2008) Probing the organization of photosystem II in photosynthetic membranes by atomic force microscopy. *Biochemistry 47*, 431–440.

97. Kirchhoff, H. (2008) Molecular crowding and order in photosynthetic membranes. *Trends Plant Sci. 13*, 201–207.

98. Kirchhoff, H., Haferkamp, S., Allen, J. F., Epstein, D. B. A., and Mullineaux, C. W. (2008) Protein diffusion and macromolecular crowding in thylakoid membranes. *Plant Physiol. 146*, 1571–1578.

99. Kirchhoff, H., Mukherjee, U., and Galla, H. J. (2002) Molecular architecture of the thylakoid membrane: Lipid diffusion space for plastoquinone. *Biochemistry 41*, 4872–4882.

100. Buzhynskyy, N., Hite, R. K., Walz, T., and Scheuring, S. (2007) The supramolecular architecture of junctional microdomains in native lens membranes. *EMBO Rep. 8*, 51–55.

101. Goncalves, R. P., Buzhynskyy, N., Prima, V., Sturgis, J. N., and Scheuring, S. (2007) Supramolecular assembly of VDAC in native mitochondrial outer membranes. *J. Mol. Biol. 369*, 413–418.

102. Stroh, C., Wang, H., Bash, R., Ashcroft, B., Nelson, J., Gruber, H., Lohr, D., Lindsay, S. M., and Hinterdorfer, P. (2004) Single-molecule recognition imaging-microscopy. *Proc. Natl. Acad. Sci. U.S.A. 101*, 12503–12507.

103. Ando, T., Uchihashi, T., Kodera, N., Yamamoto, D., Miyagi, A., Taniguchi, M., and Yamashita, H. (2008) High-speed AFM and nano-visualization of biomolecular processes. *Pfluegers Arch. 456*, 211–225.

104. Hinterdorfer, P., and Dufrene, Y. F. (2006) Detection and localization of single molecular recognition events using atomic force microscopy. *Nat. Methods 3*, 347–355.

105. Muller, D. J. (2008) AFM: A nanotool in membrane biology. *Biochemistry 47*, 7986–7998.

106. Kassies, R., Van der Werf, K. O., Lenferink, A., Hunter, C. N., Olsen, J. D., Subramaniam, V., and Otto, C. (2005) Combined AFM and confocal fluorescence microscope for applications in bio-nanotechnology. *J. Microsc. (Oxford, U.K.) 217*, 109–116.